nature catalysis

Article

https://doi.org/10.1038/s41929-023-01062-8

Tuning the thermal activation atmosphere breaks the activity–stability trade-off of Fe–N–C oxygen reduction fuel cell catalysts

In the format provided by the authors and unedited

Table of Contents

Nomenclature

Abbreviation	Description
	Characterizations
PEMFC	Proton-exchange membrane fuel cell
MEA	membrane electrode assembly
RDE	rotating disk electrode
$E_{1/2}$	Half-wave potential, the unit is V vs. RHE
j_k	Kinetic current density obtained by Koutecky - Levich equation, mA cm^{-2}
AST	Accelerated stress test
CV	Cyclic voltammetry
BOL	Beginning of life
EOL	End of life
SD	active site density, mol g_{cat}^{-1}
SEM	Scanning electron microscopy
XAS	X-ray absorption spectroscopy
XANES	X-ray absorption near edge structure spectroscopy
EXAFS	Extended X-ray absorption fine structure spectroscopy
FT-EXAFS	Fourier-transformed extended k^2-weighted extended XAFS
HAADF-STEM	High angular-dark-field scanning transmission electron microscopy
EDS	Energy dispersive spectroscopy
XPS	X-ray photon electron spectroscopy
IS	Isomer shift in ^{57}Fe Mössbauer spectroscopy, mm s^{-1}
QS	Quadrupole splitting in ^{57}Fe Mössbauer spectroscopy, mm s^{-1}
BET theory	Brunauer – Emmett – Teller theory
ICP-OES	Inductively Coupled Plasma Optical Emission spectroscopy
	Synthesis
FG	Forming gas that contains H_2 with a content from 2 to 10 mol.% in Ar
Ar	Argon gas
PGM	Platinum group metal, including Pt, Pd, Ru, Rh, Os, Ir
ZIF-8	Zeolite imidazole framework
Fe-N-C-Ar	Fe-N-C catalyst prepared in the pyrolysis in Ar
Fe-N-C-n%FG	Fe-N-C catalyst prepared in the pyrolysis in n% H_2 in Ar (n=2, 5, 10)

Catalyst synthesis, activity, and stability

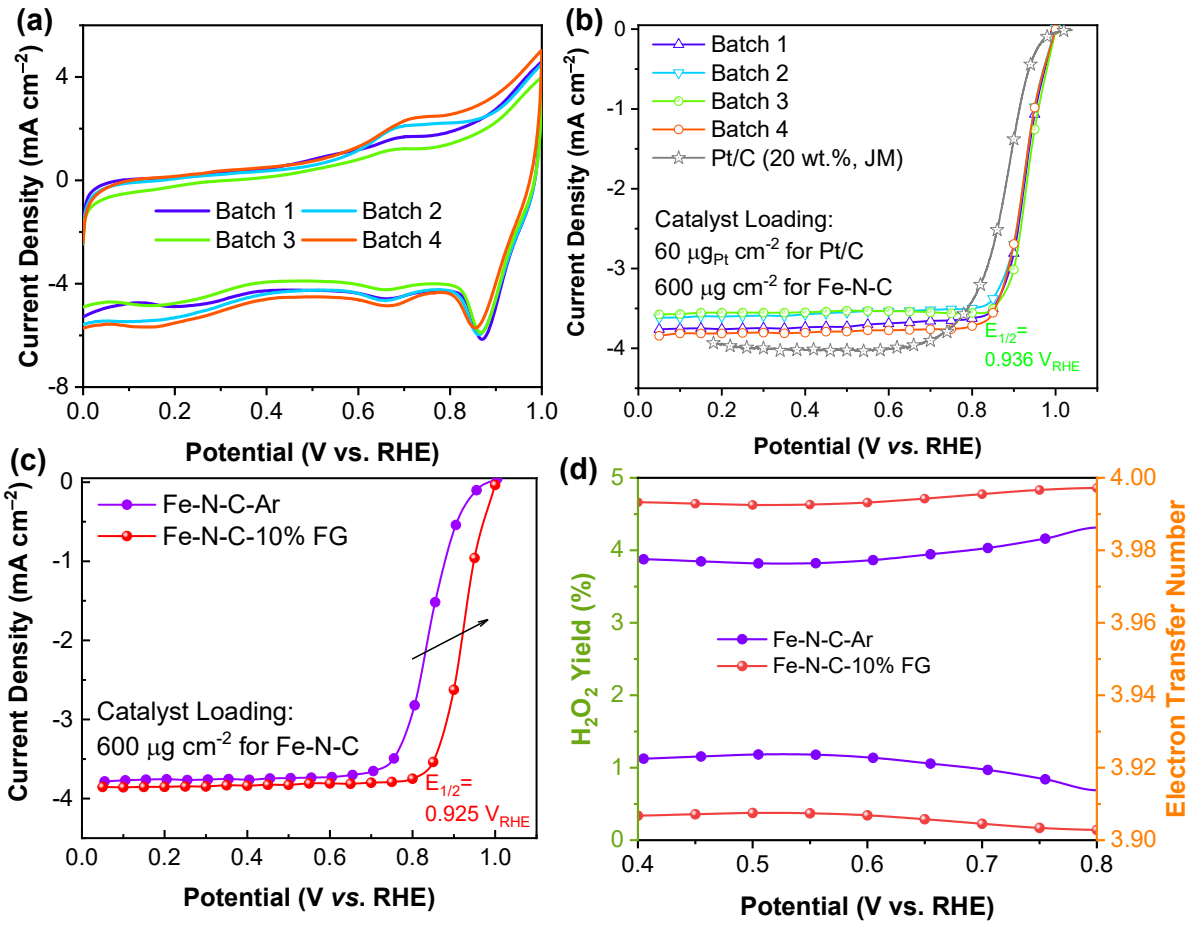

Supplementary Figure 1. Electrochemical measurements of the studied Fe-N-C catalysts. (a, b) Reproducibility of the ORR activity of Fe-N-C-10%FG prepared in the different batches. (c) Comparison of the ORR activities of Fe-NC-Ar and Fe-NC-10%FG evaluated by SCV method; the catalyst loadings were 0.6 mg cm^{-2}. (d) Comparison of H_2O_2 yield and electron transfer number of Fe-NC-Ar and Fe-NC-10%FG.

Supplementary Table 1. Comparison of the Fe-N-C catalysts prepared from reductive pyrolysis with different precursors and heating parameters.

Catalyst	Precursors	Preparation Steps	Refs.
(Fe, Fe)$_2$ + N_2/H_2	Sulfur, FeTMPPCl, iron-oxalate dihydrate	**HT1:** 7.5 °C min^{-1}, 450 °C for 10 min, 800 °C for 45 min, in Ar **AL1:** 1 M HCl for 5 h **HT2:** 10 °C min^{-1}, 800 °C for 20 min in 10% H_2/N_2 **AL2:** 1 M HCl for 1 h	Kramm et al.[1]
Fe/N/C	iron-oxalate, furnace black (71 m^2 g^{-1})	**HT:** 950 °C in NH_3 (30-35% weight loss)	Jaouen et al.[2]
Fe-N-C-H_2	Fe-poly(1,8-diaminonaphthalene)	**HT:** 400 °C at a rate of 5 °C min^{-1} and maintained for 1 h, then the temperature was increased to 900 °C at a rate of 1 °C min^{-1} and maintained for 2 h, in 10% H_2/Ar	Bao et al.[3]
12 Fe−N−C	Nicarbazin, silica, $Fe(NO_3)_3{\cdot}9H_2O$	**HT1:** 30 °C min^{-1} from 525 to 900 °C, then 10 °C min^{-1} from 900 to 975 °C, 975 °C for 45 min, in 7% H_2/N_2 **AL:** 40% HF for 4 days **HT2:** 950 °C for 30 min, in 10% NH_3/N_2	Artyushkova et al.[4]
Fe-H_2	Nicarbazin, silica, $Fe(NO_3)_3{\cdot}9H_2O$, a charge transfers organic salt	**HT1:** 30 °C min^{-1} from 525 to 900 °C, then 10 °C min^{-1} from 900 to 975 °C, 975 °C for 45 min, in 7% H_2/N_2 **AL:** HF/H_2O 2:1 for 96 hours **HT2:** 950 °C for 30 min, in 10% NH_3/N_2	P. Atanassov et al.[5]
Fe-N-C	ferrocene@ZIF-8	**HT:** 5 °C min^{-1}, 900-1100 °C for 2 hours, in 10% H_2/Ar	Li et al. [6]
Fe-N-C-10%FG	Fe_2O_3-doped ZIF-8	**HT:** 30.0 °C min^{-1}, 1100 °C for 1 hour in 10% H_2/Ar	This work

*Note: HT stands for Heat Treatment, AL stands for Acid Leaching.

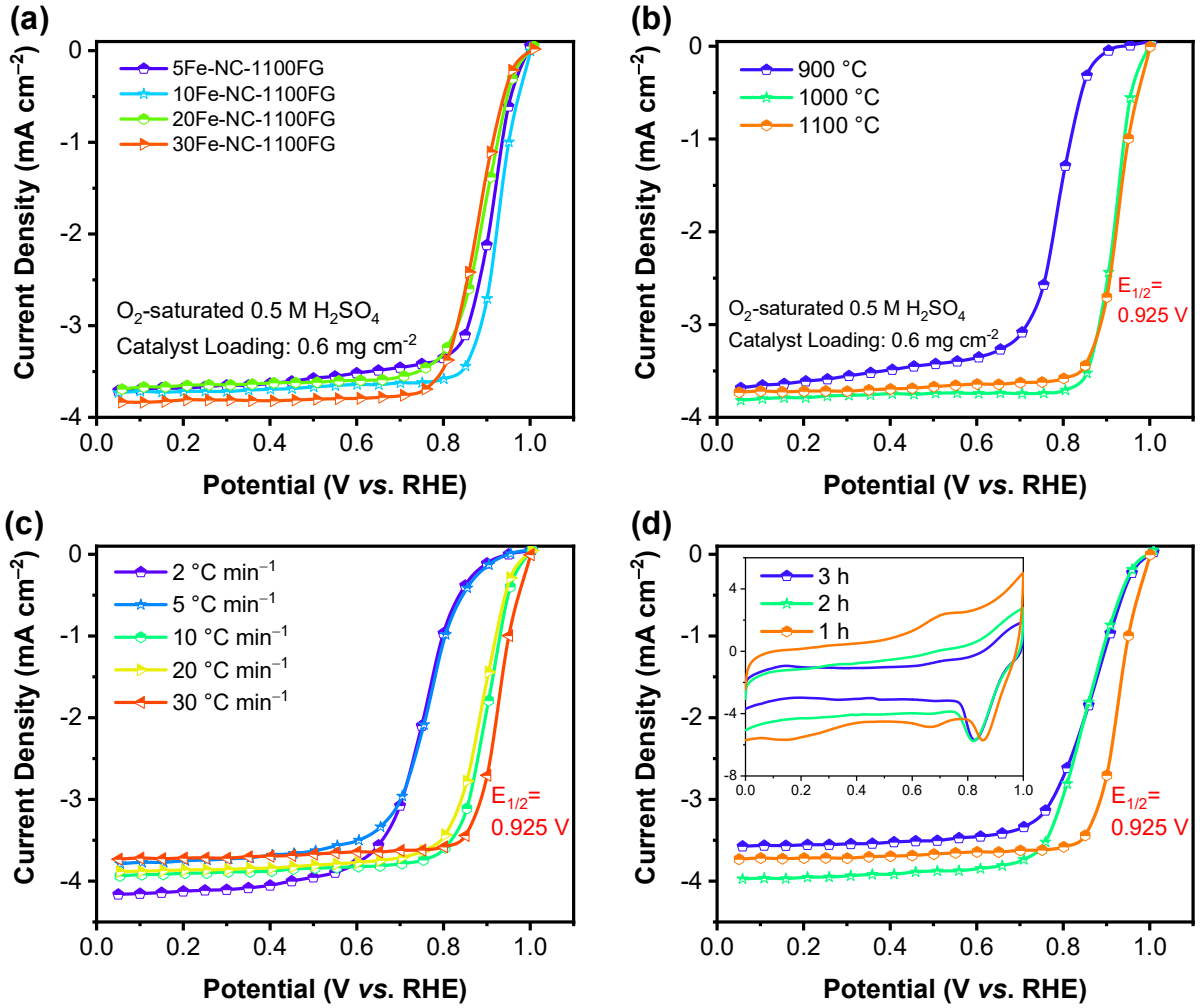

Supplementary Figure 2. Effects of the synthetic parameters on the ORR activities. (a) effects of the Fe_2O_3 NPs on the ORR performance, the *n* in the *n*Fe-NC denotes the amount of Fe_2O_3 NPs (in mg) used in the synthesis. (b) Impact of thermal annealing temperature on the ORR performance, in which an identical amount of $10Fe_2O_3$-ZIF was pyrolyzed in the 10% H_2/Ar at different temperatures for one hour. (c) Impact of heat ramping rate on the ORR performance, from which a high ramping rate contributes to high ORR performance. (d) Effect of thermal annealing duration on the ORR performance, from which a prolonged heating duration leads to a decrease in the CV profiles and ORR activity.

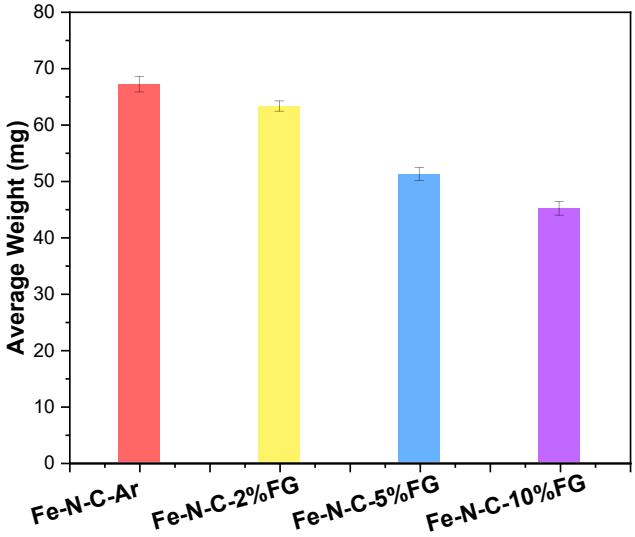

Supplementary Figure 3. Yield of the Fe-N-C catalysts obtained in different atmospheres. Error bars are calculated based on three independent experiments in each pyrolysis atmosphere. Identical heating parameters and precursors were employed.

Supplementary Table 2. Yields of the catalysts prepared from three batches of pyrolysis in different atmospheres.

Samples	Weight 1 (mg)	Weight 2 (mg)	Weight 3 (mg)	Average (mg)
Fe-N-C-Ar	65.7	67.5	68.4	67.2
Fe-N-C-2%FG	62.3	64.1	63.5	63.3
Fe-N-C-5%FG	51.2	50.0	52.3	51.2
Fe-N-C-10%FG	45.3	43.8	46.2	45.1

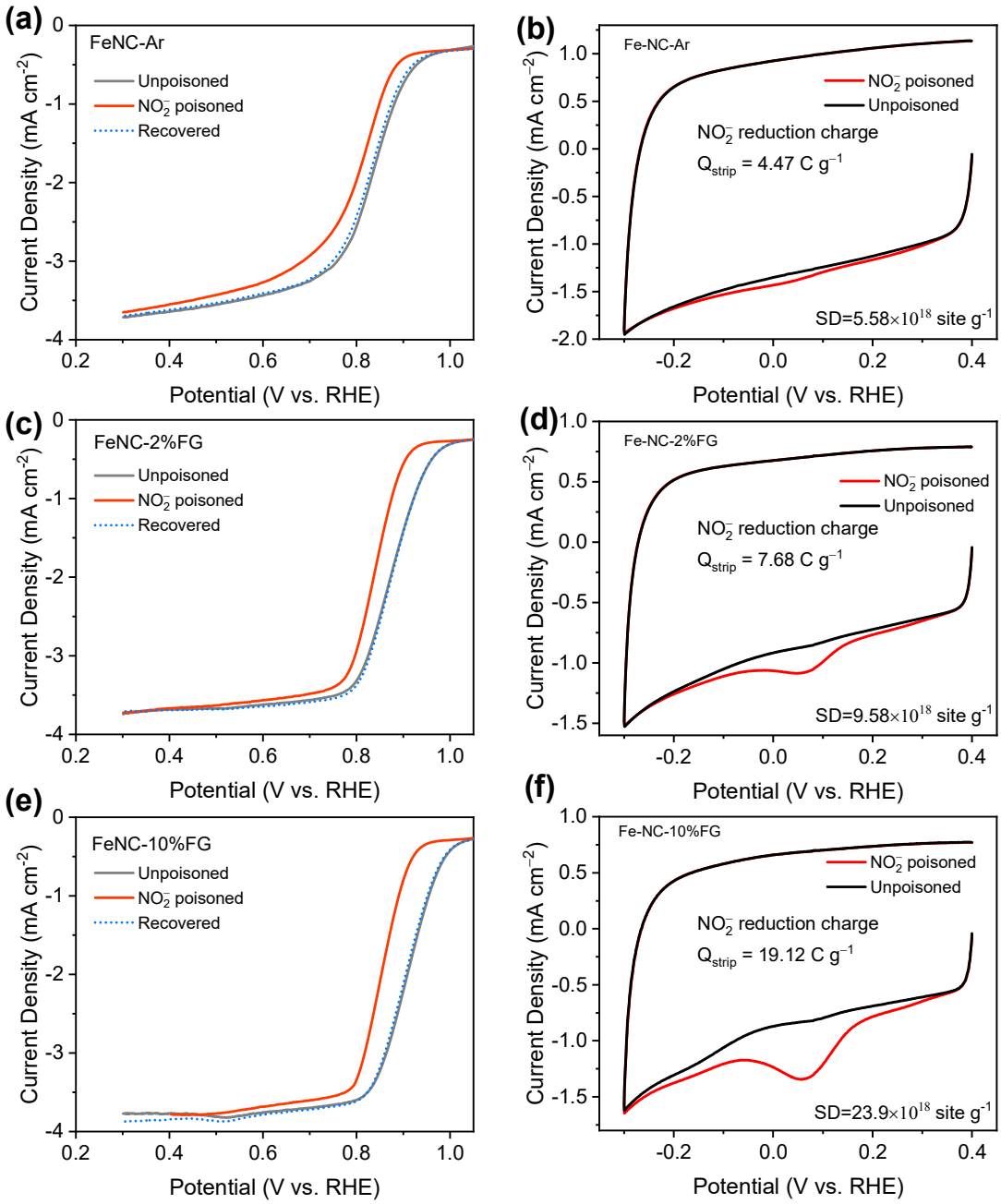

Supplementary Figure 4. Determination of FeN_4 site densities of the Fe-N-C catalysts. Left column, LSV curves before, during, and after nitrite adsorption in a 0.5 M acetate buffer at pH 5.2 for Fe-N-C-Ar (a), Fe-N-C-2%FG (c) and Fe-N-C-10%FG (e) catalysts. Right column, CV curves before and after nitrite stripping in the nitrite reductive stripping region for Fe-N-C-Ar (b), Fe-N-C-2%FG (d), and Fe-N-C-10%FG (f) catalysts. Catalyst loading: 0.20 mg cm^{-2}.

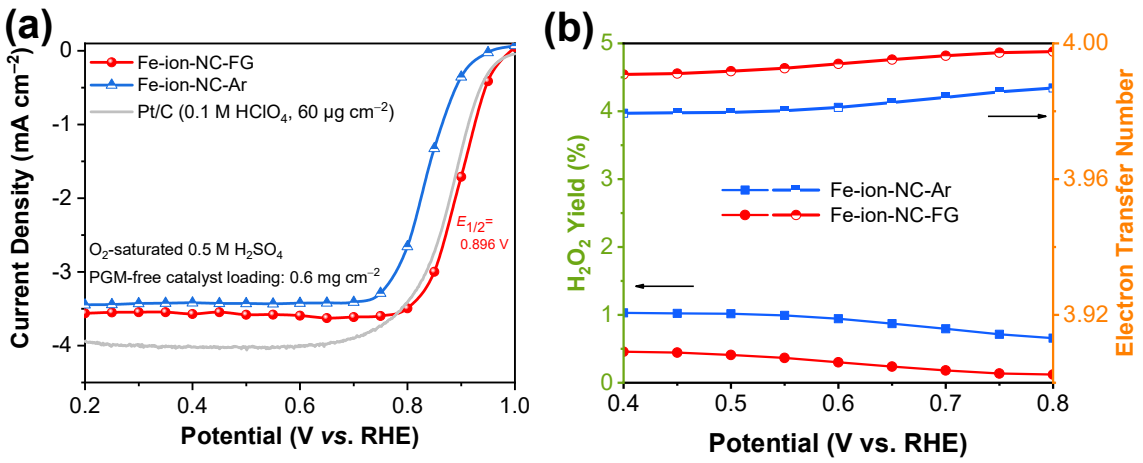

Supplementary Figure 5. Electrochemical measurements of Fe-ion-NC catalysts. The Fe-ZIF was prepared by chemically doping Fe ions in the ZIF-8. (a) ORR activities of Fe-ion-NC-Ar and Fe-ion-NC-FG evaluated by SCV method. The catalyst loadings were 0.6 mg cm^{-2}. The performance of Pt/C (60 μg_{Pt} cm^{-2}) was served as baseline. (b) Comparison of H_2O_2 yield and electron transfer number of Fe-ion-NC-Ar and Fe-ion-NC-FG.

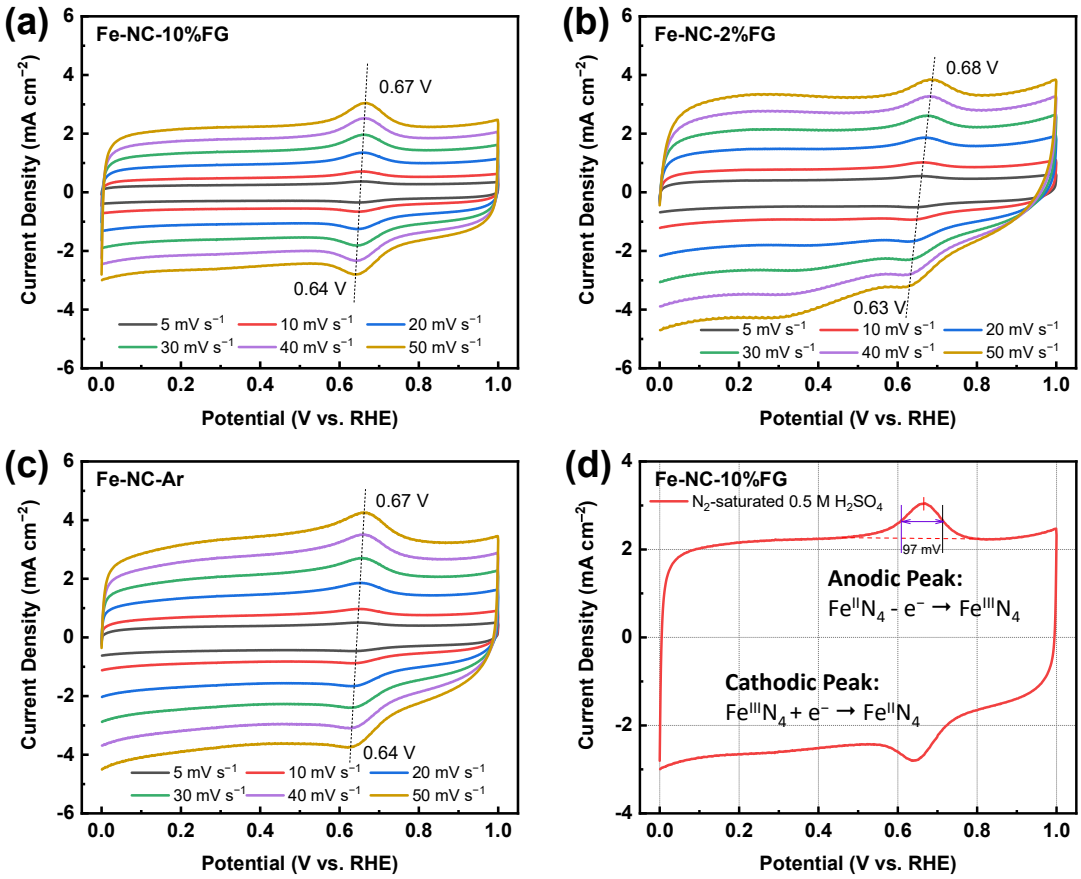

Supplementary Figure 6. CV profiles of the Fe-N-C catalysts in the N_2-saturated 0.5 M H_2SO_4. (a, b, c) Comparison of the CV profiles of Fe-N-C-Ar (a), Fe-N-C-2%FG (b), and Fe-N-C-10%FG (c) recorded in the N_2-saturated 0.5 M H_2SO_4 at different scanning rate. (d) Elucidation of the electrochemical process for each peak in the CV profile of Fe-N-C-10%FG.

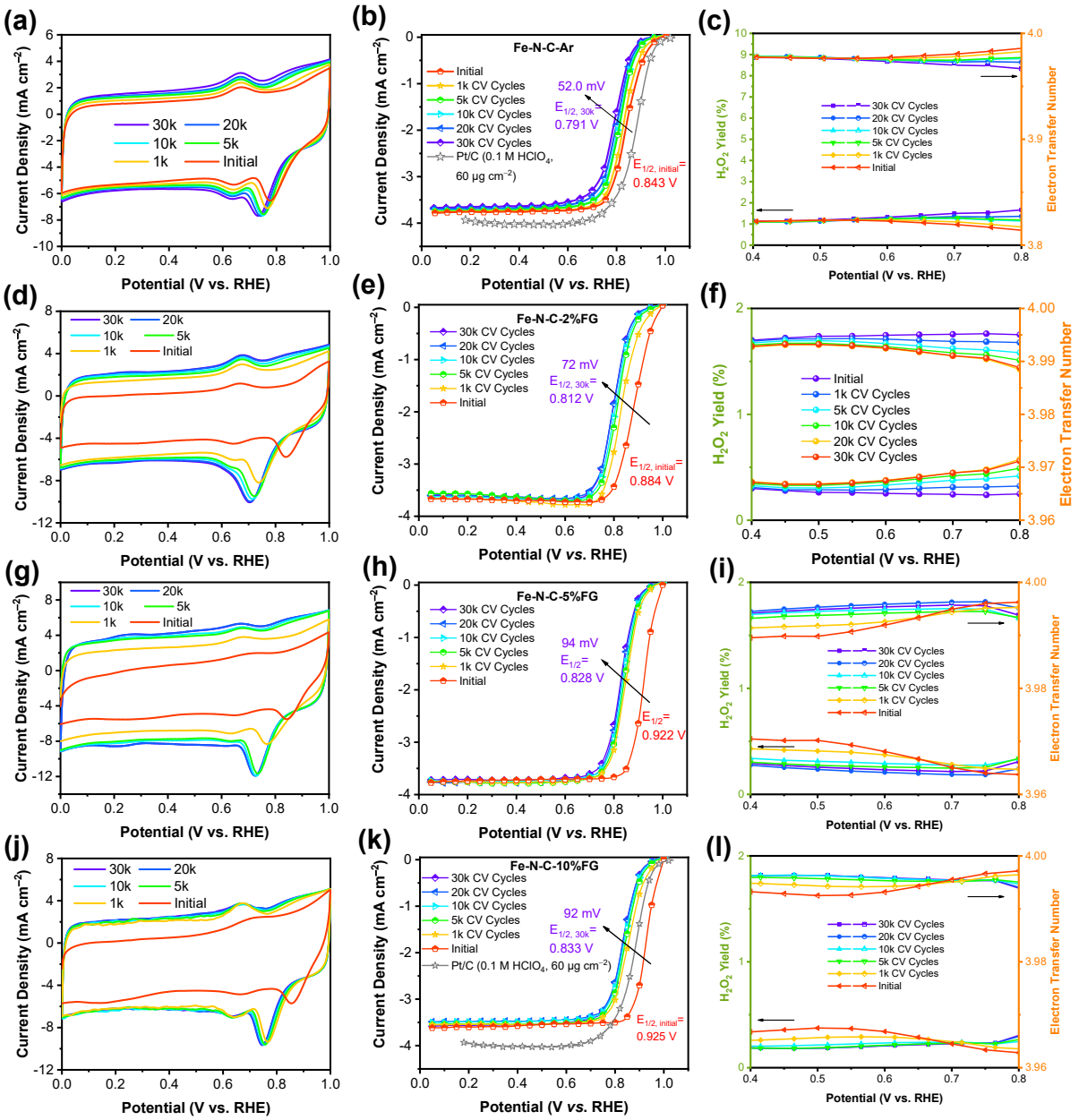

Supplementary Figure 7. Effects of pyrolysis atmosphere on activity and durability of Fe-N-C catalysts. (a, d, g, j) CVs of the Fe-N-C-Ar (a), Fe-N-C-2%FG (d), Fe-N-C-5%FG (g), and Fe-N-C-10%FG (j) during 30,000 cycles of accelerated stress test (AST), the scanning rate is 50 mV s^{-1}. (b, e, h, k) Evolutions of ORR activities of the Fe-N-C-Ar (b), Fe-N-C-2%FG (e), Fe-N-C-5%FG (h), and Fe-N-C-10%FG (k) during the AST. (c, f, i, l) The variation of H_2O_2 yields and electron transfer numbers of the Fe-N-C-Ar (c), Fe-N-C-2%FG (f), Fe-N-C-5%FG (i), and Fe-N-C-10%FG (l) during the AST. The AST was performed by sweeping the potential in the range of 0.6 to 0.95 V_{RHE}. The scanning rate is 50 mV s^{-1}, and the electrolytes were O_2-saturated 0.5 M H_2SO_4. After certain cycles, CVs and SCVs were recorded. During the SCV recording, the ring potential was held at 1.1 V_{RHE} to detect the yield of H_2O_2.

Fuel cell MEA performance

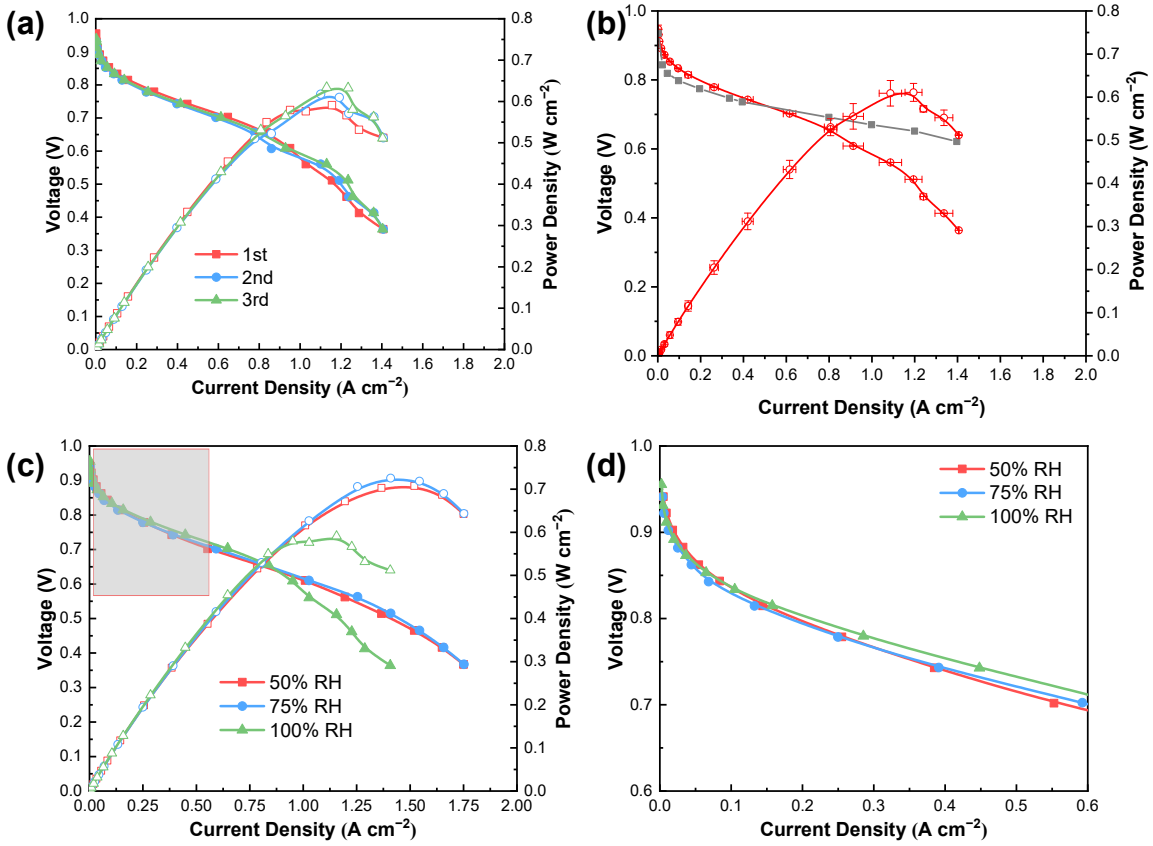

Supplementary Figure 8. H_2-air fuel cell performance of Fe-N-C-FG under different conditions. (a) H_2-air fuel cell I-V polarization (solid symbols and lines) and power density (hollow symbols and lines) recorded under 150 kPa_{abs} of air pressure, the relative humidity is 100%, the cathode of Fe-N-C-FG and commercial Pt/C at the flow rate of air 700/1700 sccm (H_2/air). (b) I-V curve with error bar obtained from a). (c, d) H_2-air fuel cell I-V polarization of Fe-N-C-10%FG under different RHs. The cathode loading is ca. 4.5 mg cm^{-2}; 0.6 I/C; 150 kPa_{abs} backpressure. Anode: Pt/C, 0.10 mg_{Pt} cm^{-2}; 150 kPa_{abs} backpressure. Membrane: Gore™ membrane (15 μm). The error bars represent the standard derivation derived from three separate tests.

Supplementary Table 3. Comparison of fuel cell performance in three measurements. The cathode loading is ca. 4.5 mg cm^{-2}; 100 % RH; 0.6 I/C; 150 kPa_{abs} backpressure. Anode: Pt/C, 0.10 mg_{Pt} cm^{-2}, 100% RH; 150 kPa_{abs} backpressure. Membrane: Gore™ membrane. Cell temperature: 80 °C. MEA area: 5.0 cm^2. Differential fuel cell with 14 parallel flow channels.

Number of Cycles	Current Density at 0.8 V (mA cm^{-2}) in H_2-air	Power Density @ 0.67 V (mW cm^{-2}) in H_2-air
1st cycle	**211.0**	**525.0**
2nd cycle	176.0	504.0
3rd cycle	186.0	482.0
Average	**191.0**	**501.0**

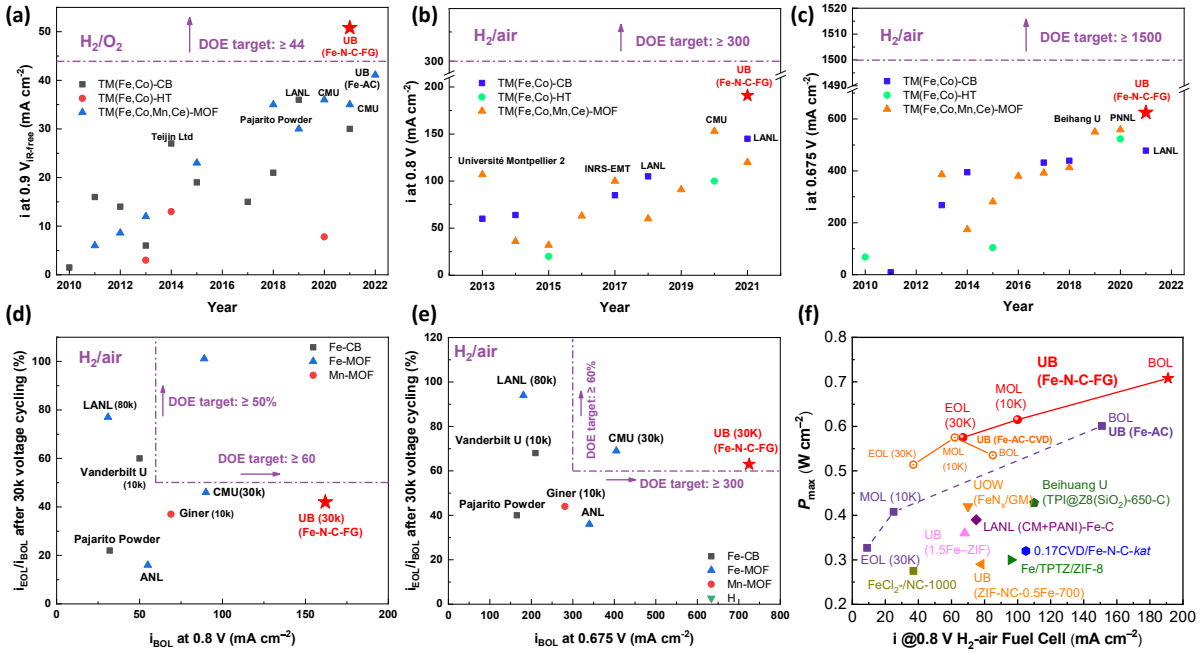

Supplementary Figure 9. H_2-fuel cells performance benchmarks of Fe-N-C-cathodes. (a-c) Comparison of the initial performance of Fe-N-C-10%FG with the reported Fe-N-C catalysts in H_2-O_2 by 2023. (a) and H_2-air (b-c) fuel cells. (d-f) Performance of Fe-N-C-10%FG and the reported Fe-N-C catalysts during the durability tests. The performance was recorded by following the latest U.S. ElectroCat Consortium protocols,[7] in which new DOE targets have been released. In Figure (a), TM: transition metal; CB: carbon black; HT: hard template.

Supplementary Table 4. Summary of electrochemical performance of the previously reported Fe−N−C catalysts.

Catalysts	j_k/A g^{-1}	$E_{1/2}$/ V *vs*. RHE	Electrolyte disk rotation rate/rpm	Fuel cell performance		Ref.
				Current density @0.9 V/mA cm^{-2}, H_2−O_2	Current density @0.8 V /mA cm^{-2}, H_2−air	
Fe−N-C-FG	**18.8**	**0.925**	**0.5 M H_2SO_4, 900**	**50.8**	**191.0**	**This work**
Fe-N-C-AC		0.915	0.5 M H_2SO_4, 900	44.2	151	[8]
0.17CVD/Fe−N−C−*kat*		0.835	0.5 M H_2SO_4, 900	27	105	[9]
(CM+PANI) Fe−C	0.066	0.80	0.5 M H_2SO_4, 900	16	75	[10]
Zn(eIm)$_2$TPIP		0.78	0.1 M $HClO_4$, 1600	–	–	[11]
Fe−PAN−EN hydrogel		0.83	0.5 M H_2SO_4, 900	–	–	[12]
1.5Fe−ZIF		0.88	0.5 M H_2SO_4, 900	18	68	[13]
TPI@Z8(SiO_2)−650−C		0.823	0.5 M H_2SO_4, 1600	22	105	[14]
Fe/TPTZ/ZIF−8		–	–	4	96	[15]
ZIF−NC−0.5Fe−700		0.84	0.5 M H_2SO_4, 900	30	78	[16]
FeN_x/Gp		0.80	0.5 M H_2SO_4, 900	13	70	[17]
$FeCl_2$−/NC−1000		0.80	0.1 M $HClO_4$, 1600	15	37	[18]

Supplementary Table 5. The impact of relative humidity on fuel cell performance. The 1st I-V curve was used for comparison to eliminate the effect of accumulated water in the MEA. The humidity was modulated from low to high.

RH	Peak Power Density (mW cm^{-2}) in air	Power Density @ 0.67 V (H_2/Air, mW cm^{-2})
50 %	725.0	481.0
75 %	705.0	502.0
100 %	591.0 (flooding)	526.0

Supplementary Table 6. H_2-air fuel cell performance of Fe-N-C-Ar cathode during the AST. The anode and cathode were purged with H_2/air at flow rates of 700 and 1700 sccm under 150 kPa_{abs} pressure.

Fe-N-C-Ar	Current density @ 0.80 V, mA cm^{-2}	Current density @ 0.67 V, mA cm^{-2}
BOL	109.0	474.5
EOL	11.0	118.6

Supplementary Table 7. Comparison in current density loss at 0.8 V and peak power density loss in H_2-air cell for the Fe-N-C-10%FG cathodes.

Fe-N-C-FG	Current density @ 0.80 V (H_2/air, mA cm^{-2})	Voltage @ 0.8 A cm^{-2} (mV)	Peak Power Density (H_2/air, mW cm^{-2})	Power Density@ 0.67 V (H_2/air, mW cm^{-2})
BOL	191.0	659.3	725.3	502.0
5k	130.0	642.6	659.2	452.3
10k	100.0	614.9	609.4	379.2
20k	79.0	586.0	545.1	335.7
30k	67.0	574.7	529.7	306.8
Loss	64.9 %	12.7 %	27.0 %	38.9 %

Note: Average current density at 0.8 V obtained from Supplementary Figure 8 (b) was used for BOL performance.

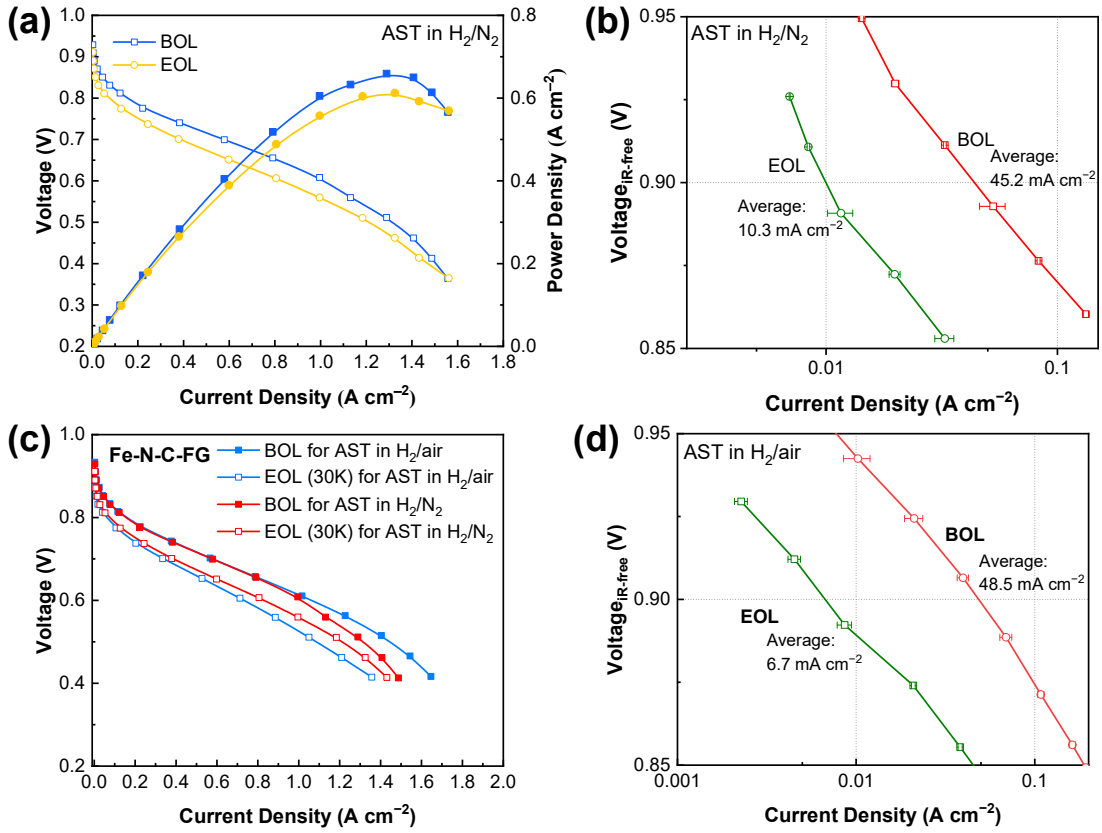

Supplementary Figure 10. Effects of AST in the H_2/air or H_2/N_2 conditions on the MEA stability. (a) H_2-air fuel cell polarization plots and (b) Determination of current densities @ $0.9V_{iR\text{-}free}$ of Fe-N-C-10%FG cathodes recorded before (BOL) and after 30,000 cycles AST in H_2/N_2 condition. (c) Comparison of the fuel cell performance of Fe-N-C-10%FG cathode after the AST in H_2/N_2 and H_2/air atmosphere. (d) Determination of current densities @ $0.9V_{iR\text{-}free}$ of Fe-N-C-10%FG cathodes recorded before and after 30,000 cycles AST in H_2/air condition. AST square-wave voltage cycles in H_2/N_2 and H_2/Air cells between 0.60 and 0.95 V under 150 kPa_{abs} and flow rates of 400 sccm N_2 (or air) and 200 sccm for H_2. The H_2-air fuel cell performance were obtained by purging the anode and cathode with H_2/air at flow rates of 700 sccm (H_2) and 1700 sccm (air) under 150 kPa_{abs} pressure, the cell temperature was 80 °C, the relative humidity was 75 %. The error bars represent the standard derivation derived from three separate tests.

Supplementary Table 8. Comparison in performance loss in H_2-air MEA after ASTs using 30,000 voltage cycles in H_2/air or H_2/N_2 for the Fe-N-C-10%FG cathodes.

	Fe-N-C-10%FG, 150 kPa_{abs}		
	Current density loss @ 0.8 V (mA cm^{-2})	Current density loss @ 0.67 V (mA cm^{-2})	Peak power density loss (mW cm^{-2})
AST in H_2-N_2	78.	201	46
AST in H_2-Air	124	289	176

Catalyst Characterization for Mechanistic Understanding

Supplementary Table 9. Parameters derived from the fittings of ^{57}Fe Mössbauer spectra. Isomer shift (**δ**), quadrupole splitting (**QS**, line width (**Γ**), and relative absorption spectral area (%). The first column features the component of each Fe species in these spectra.

Component	δ mm s^{-1}	QS mm s^{-1}	Γ mm s^{-1}	Field T	Area %	Assignment
	^{57}Fe-N-C-Ar, 295 K					
D1	0.32 (0.0038)	1.29 (0.0074)	0.85 (0.0154)	-	54.3 (1.79)	High-spin $Fe^{III}N_4C_{12}$-site[19-21]
D2	0.5 (0.0118)	2.62 (0.0616)	1.74 (0.066)	-	34.8 (2.13)	Low- or intermediate-spin $Fe^{II}N_4C_{10}$ site[19-21]
Singlet	-0.094 (0.0076)	-	0.3 (0.0236)	-	1.6 (0.47)	γ-Fe[22]
Sextet 1	-0.036 (0.0124)	0	0.64 (0.0384)	33.6 (0.085)	7.0 (0.47)	α-Fe
Sextet 2	0.22 (0.0137)	-0.06 (0.0257)	0.34 (0.0474)	21.2 (0.0944)	2.3 (0.19)	Fe_3C
	^{57}Fe-N-C-10%FG, 295 K					
D1	0.3 (0.0134)	1.21 (0.023)	0.79 (0.0676)	-	28.7 (4.72)	High-spin $Fe^{III}N_4C_{12}$-site[19-21]
D2	0.42 (0.0233)	2.3 (0.1991)	1.83 (0.1369)	-	31.1 (4.72)	Low- or intermediate-spin $Fe^{II}N_4C_{10}$ site[19-21]
Singlet	-0.097 (0.0035)	-	0.52 (0.0117)	-	17.5 (0.47)	γ-Fe[22]
Sextet 1	0.0	0.0	0.55 (0.0171)	33.8 (0.0365)	20.0 (0.62)	α-Fe
Sextet 2	0.2 (0.0235)	-0.062 (0.0465)	0.42 (0.0827)	21.4 (0.1567)	2.6 (0.72)	Fe_3C
	$(Fe,Fe)_1 + N_2/H_2$ catalysts, 295 K, *Kramm, U. I. et al., J. Am. Chem. Soc. 2016, 138 (2), 635-640.*					
D1	0.32 (0.03)	0.81 (0.08)	0.63 (0.06)		49.2	$Fe^{II}N_4$-site, Low-spin
D2	0.36 (0.04)	2.53 (0.33)	1.08 (0.30)		33.8	Pc-type $Fe^{II}N_4$-site, mid-spin
D3	0.35 (0.05)	1.36 (0.17)	0.69 (0.06)		17.0	Porph-type $Fe^{II}N_4$-site, mid-spin
Singlet	0.00 (0.14)	-	0.35 (0.07)		0.0	Superparamagnetic α-Fe
Sextet 1	0.04 (0.02)	-	0.60 (0.01)	35.3 (0.2)	0.0	α-Fe
Sextet 2	0.34 (0.02)	-	1.13 (0.12)	48.3 (0.6)	0.0	Iron nitride

Supplementary Table 10. Parameters derived from the fittings of ^{57}Fe Mössbauer spectra. Isomer shift (**δ**), quadrupole splitting (**QS**), line width (**Γ**) and relative absorption spectral area (%). The first column features the component of each Fe species in these spectra.

Component	δ mm s^{-1}	QS mm s^{-1}	Γ mm s^{-1}	Field T	Area %	Assignment
	^{57}Fe-N-C-Ar, 6.5 K					
D1	0.49 (0.0014)	0.99 (0.0048)	0.83 (0.0093)	-	54.1 (1.2)	High-spin $Fe^{III}N_4C_{12}$-site[19-21]
D2	0.52 (0.0058)	2.43 (0.0416)	1.54 (0.0378)	-	31.9 (1.38)	Low- or intermediate-spin $Fe^{II}N_4C_{10}$ site[19-21]
Singlet	0.0	-	0.5	-	1.7 (0.1)	γ-Fe[22]
Sextet 1	0.076 (0.0059)	0.056 (0.0116)	0.43 (0.0195)	33.8 (0.0393)	6.3 (0.31)	α-Fe
Sextet 2	0.33 (0.0079)	-0.013 (0.015)	0.5 (0.0247)	25.4 (0.0498)	6.0 (0.31)	Fe_3C
	^{57}Fe-N-C-10%FG, 6.5 K					
D1	0.59 (0.0021)	0.82 (0.0049)	0.59 (0.0094)	-	22.4 (0.91)	High-spin $Fe^{III}N_4C_{12}$-site[19-21]
D2	0.6 (0.0063)	2.05 (0.0457)	1.91 (0.0337)	-	33.4 (0.91)	Low- or intermediate-spin $Fe^{II}N_4C_{10}$ site[19-21]
Singlet	-0.058 (0.0013)	-	0.68 (0.0062)	-	23.7 (0.16)	γ-Fe[22]
Sextet 1	0.11 (0.0008)	0.014 (0.0017)	0.32 (0.0028)	34.0	17.5 (0.12)	α-Fe
Sextet 2	0.32 (0.0067)	0.0098 (0.0133)	0.39 (0.022)	25.4	3.0 (0.17)	Fe_3C

Supplementary Table 11. Lamb- Mössbauer Factors for the Mössbauer spectroscopy analysis.[19]

	Lamb-Mossbauer Factors	
Components	**298 K**	**6.5 K**
D1	0.46	0.86
D2	0.52	0.87
α-Fe	0.67	0.9
γ-Fe	0.77	0.92
Fe_3C	0.77	0.92

Supplementary Table 12. Analysis of metal contents in the ^{57}Fe-N-C catalysts. Zn and Fe contents in the catalysts prepared with $^{57}Fe_2O_3$ as determined by ICP-OES (wt.%).

Samples	Elements	Content 1 (wt. %)	Content 2 (wt. %)	Content 3 (wt. %)	Average (wt. %)
^{57}Fe-N-C-Ar	Fe	0.15	0.15	0.15	0.15
	Zn	0.10	0.10	0.10	0.10
^{57}Fe-N-C-2%FG	Fe	0.57	0.56	0.56	0.56
	Zn	n.a.	n.a.	n.a.	n.a.
^{57}Fe-N-C-10%FG	Fe	0.73	0.73	0.72	0.73
	Zn	n.a.	n.a.	n.a.	n.a.

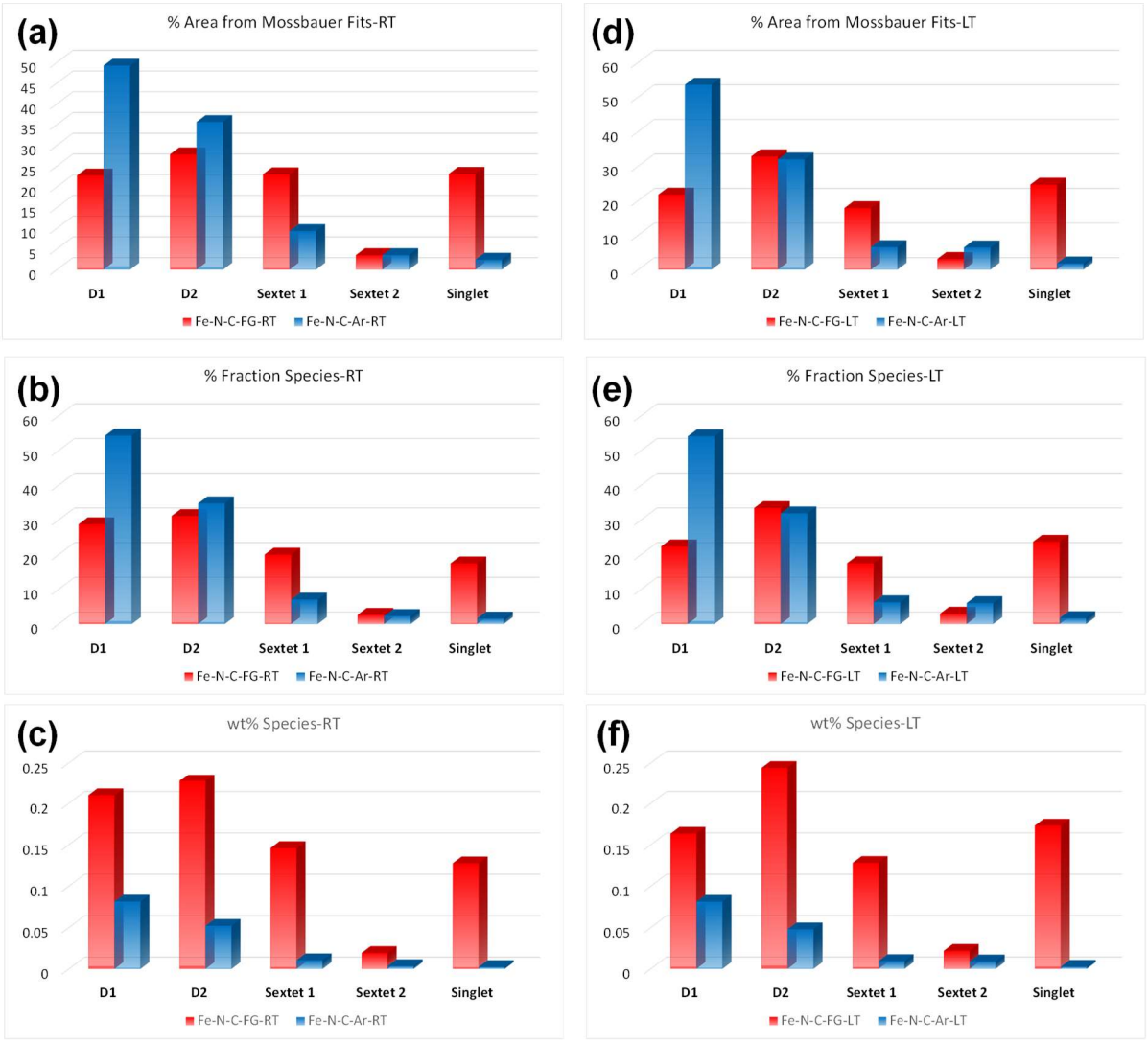

Supplementary Figure 11. Comparison of the fractions of the components of the Fe-N-C-Ar and Fe-N-C-10%FG derived from the fittings of low temperature (6.5 K) and room temperature (295 K) Mössbauer spectra.

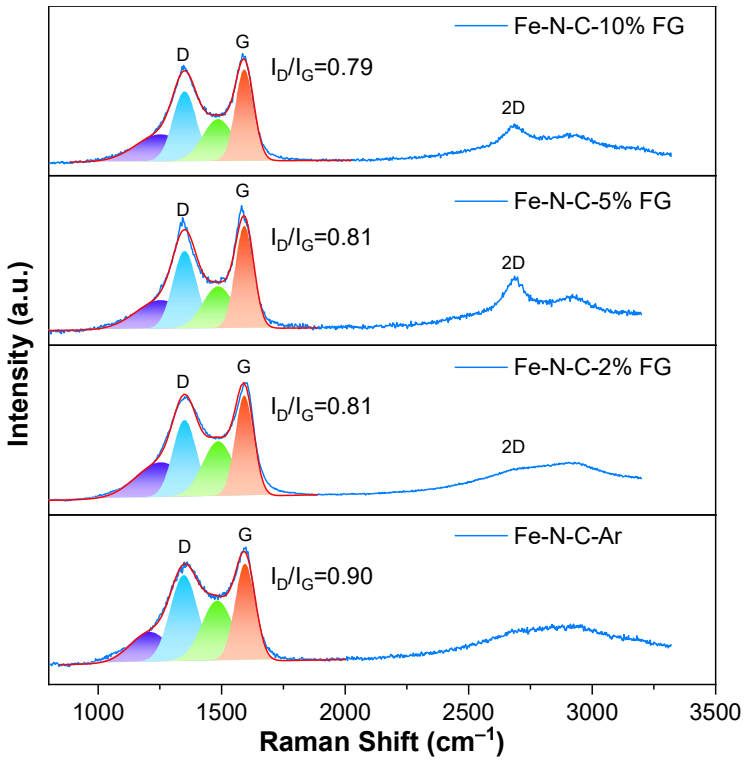

Supplementary Figure 12. Raman spectra of Fe-N-C catalysts. The heating programs were identical during the synthesis, except for the pyrolysis atmosphere**.**

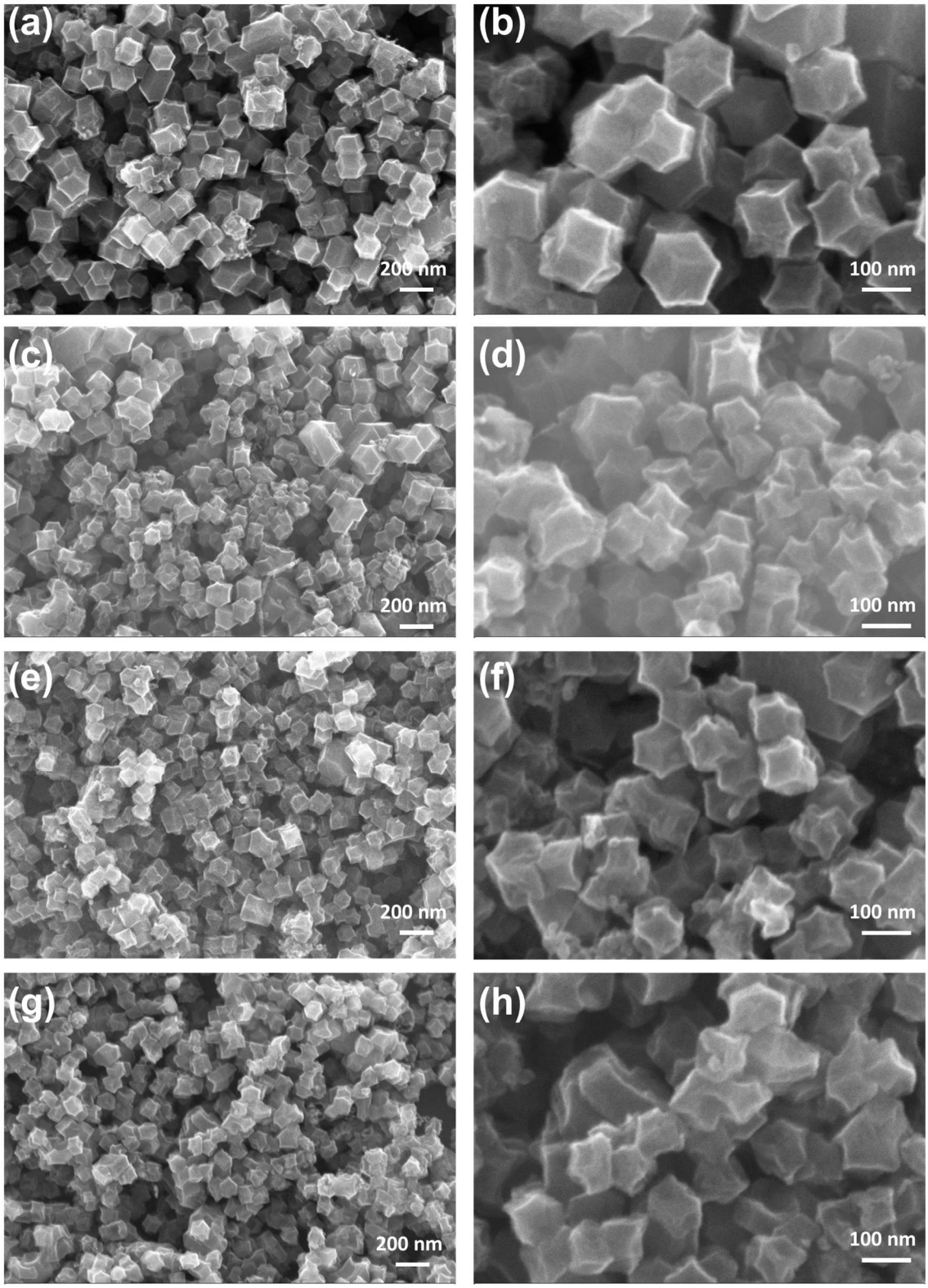

Supplementary Figure 13. Morphologies of the Fe-N-C catalysts prepared in the different atmospheres. SEM images of Fe-N-C catalysts prepared in Ar (a, b), 2 mol. % H_2 (c, d), 5 mol. % H_2 (e, f), 10 mol. % H_2 in forming gas (g, h).

Supplementary Table 13. STEM-EDS elemental quantification of Fe-N-C-Ar and Fe-N-C-10%FG catalysts prepared at 1100 ºC.

	Elemental composition (at. %)				
	C	N	O	Fe	Zn
	96.37	1.22	2.31	0.06	0.04
Fe-N-C-Ar	96.53	0.84	2.55	0.05	0.03
	96.25	1.1	2.56	0.06	0.04
Average	**96.38**	**1.05**	**2.47**	**0.06**	**0.04**
	98.19	0.51	1.28	0.03	0.00
Fe-N-C-10%FG	98.26	0.42	1.29	0.03	0.00
	98.08	0.48	1.42	0.02	0.00
Average	**98.18**	**0.47**	**1.33**	**0.03**	**0.00**

Supplementary Table 14. Pore distributions and specific BET surface areas of Fe-N-C catalysts.

Sample	V_{micro}		V_{meso}		V_{macro}		V_{total}	S_{BET}
	$cm^3\ g^{-1}$	%	$cm^3\ g^{-1}$	%	$cm^3\ g^{-1}$	%	$cm^3\ g^{-1}$	$m^2\ g^{-1}$
Fe−N-C-Ar	0.31	68.9	0.10	22.2	0.04	8.9	0.45	824.4
Fe−2%FG	0.40	62.5	0.15	23.4	0.08	12.5	0.64	1201.7
Fe−5%FG	0.38	61.3	0.17	27.4	0.07	11.3	0.62	1148.9
Fe−10%FG	0.38	52.0	0.27	37.0	0.08	11.0	0.73	1187.3

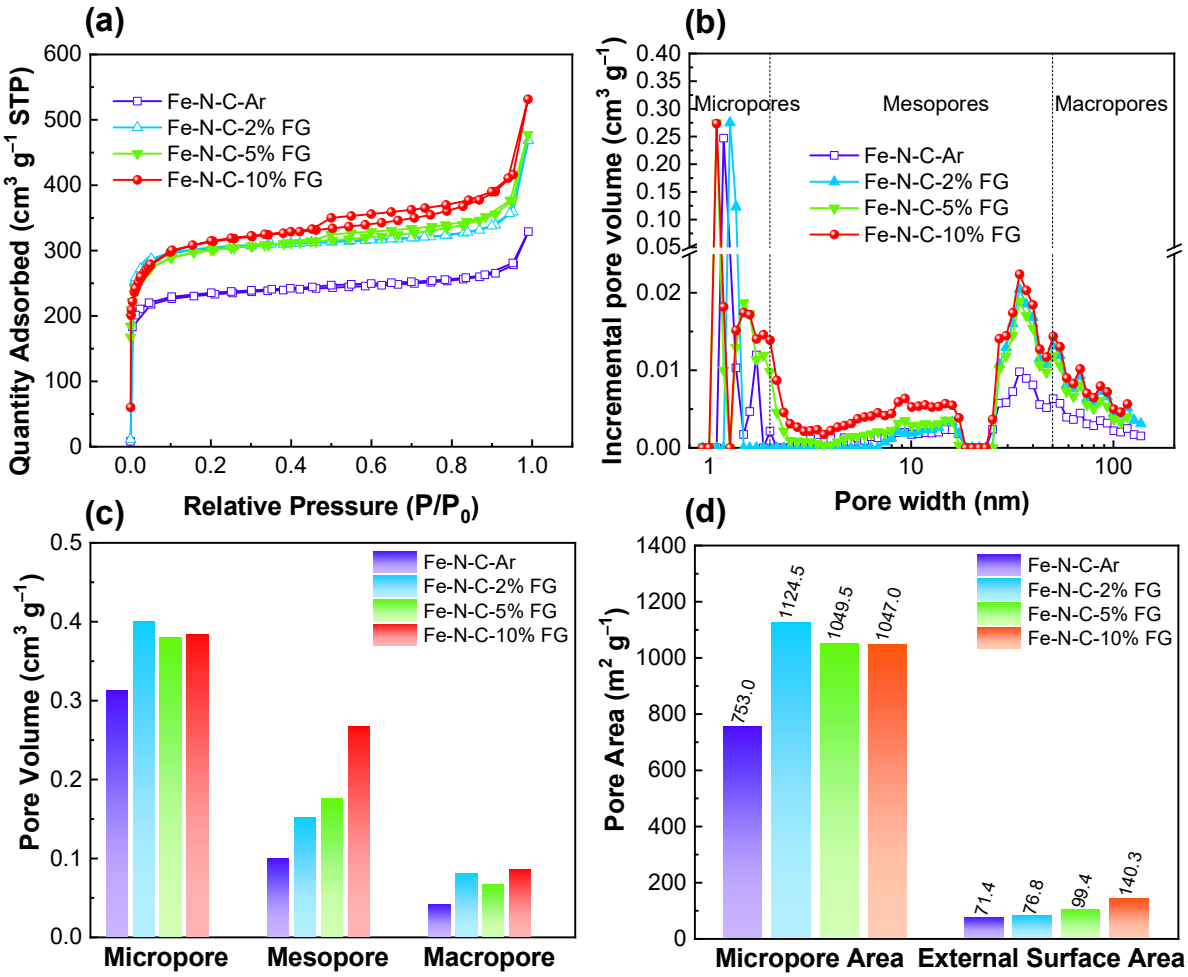

Supplementary Figure 14. Analysis of specific BET surface areas and pore distributions. (a) Isothermal N_2 adsorption/desorption plots and (b) pore distribution of Fe-N-C-Ar and Fe-N-C-FG catalysts. (c) Comparison of pore volume for the Fe-N-C catalysts. (d) Comparison of pore area distributions in Fe-N-C-Ar and Fe-N-C-FG catalysts, the micropore, and external surface area were obtained with t-plot analysis.

Supplementary Table 15. Fitting parameters obtained from FT-EXAFS analysis of Fe-N-C catalysts. CN: coordination number; R: distance; σ^2: mean-square disorder; E_0: energy shift. The single-digit numbers in parentheses are the last-digit errors.

FePc (without pyrolysis and without O_2-adsorption)					
Scattering paths	CN	R (Å)	E_0 (eV)	σ^2 (Å^2)	R-facotr
Fe-N	4	1.93(1)	−5(1)	0.0078(9)	0.018
Fe-C	8	2.96(1)		0.0078(1)	
Fe-N-C	16	3.13(2)		0.0040(6)	
Fe-N	4	3.37(2)		0.0065(8)	
Fe-N-N	16	3.86(2)		0.0008(7)	
Fe-N-N	4	3.86(2)		0.0008(7)	
Fe-C	6	4.19(2)		0.0184(6)	
Fe-N-C	12	4.22(2)		0.0107(2)	
Fe-N-C-Ar					
Scattering Paths	CN	R (Å)	E_0 (eV)	σ^2 (Å^2)	R-factor
Fe-N	4.2(0.9)	2.02(2)	0.5(1)	0.0082(8)	0.038
Fe-C	9.1(1.7)	3.04(7)		0.0197(6)	
Fe-N-C	18.2(3.5)	3.26(7)		0.0132(9)	
Fe-N-C-10%FG (Catalyst)					
Scattering Paths	CN	R (Å)	E_0 (eV)	σ^2 (Å^2)	R-factor
Fe-N	4.31(5)	1.95(3)	1.7(7)	0.003(5)	0.033
Fe-C	9.1(2)	2.91		0.003(3)	
Fe-N-C	13.6(8)	3.21(5)		0.007(1)	
Fe-N-C-10%FG (Electrode)					
Scattering Paths	CN	R (Å)	E_0 (eV)	σ^2 (Å^2)	R-factor
Fe-N	4.10(1)	1.95(1)	1.68(7)	0.01(3)	0.018
Fe-C	5.84(6)	2.96(4)		0.02(5)	
Fe-N-C	8.70(1)	3.29(1)		0.05(9)	

Supplementary Note 1:

The precursors of both Fe-N-C-Ar and Fe-N-C-FG catalysts are Fe_2O_3 nanoparticles surrounded by ZIF-8. During the heat treatment, the oxygen of Fe_2O_3 and the adsorbed oxygen molecule would react with C to mainly give CO and perhaps also some CO_2. This is the primary gasification reaction for the catalyst precursors that leads to Fe-N-C-Ar.

When H_2 is added to Ar, other gasification reactions are added to the previous one. First, H_2 will react with oxygen to yield H_2O. The latter will be able to react with carbon according to:

$$C + H_2O \rightarrow CO + ½\ H_2. \quad (1)$$

CO will further be able to react with more water according to:

$$CO + H_2O \rightarrow CO_2 + H_2. \quad (2)$$

C will also be able to react directly with H_2 according to:

$$C + 2H_2 \rightarrow CH_4. \quad (3)$$

All these reactions will multiply the gasification possibilities of the carbon support, which will react faster if this carbon support presents a significant degree of disorder as for the ill-defined graphene layers in the mesopores, while there will be only a few reactions of gasification, concentrated at weak points, for the much better organized double graphene layers.

Therefore, carbon will quickly disappear in the mesopores, justifying the 2.7 factor for the carbon loss that increased the mesopore volume at 10%H_2 in Fe-N-C-10%FG. At the same time, only weak points will be etched as micropores (having a pore width near the mesopore limit) in the double graphene layers, justifying a factor of only 1.26 found for the loss of carbon in the micropores from 2 to 10%H_2. Once the weak point has been etched, the gasification of the double graphene layers will stop. This is already occurring at 2%H_2 in the FG.

Therefore, the Fe-N-C-FG catalyst is made of a series of double graphene layers (having an inter-distance of 0.48 ± 0.10 nm separated by about 20 nm). Between these well-organized layers, several mesopores are made of ill-defined single-carbon layers. They contain a large number of defects. Fe catalytic sites for ORR are found in both types of structure.

In particular, when H_2 is added to Ar in the gas introduced during the pyrolysis, H_2 multiplies the gasification opportunities of the carbon support during the pyrolysis. Of course, the carbon layers with the lowest structural organization will react faster than the better-organized ones. This is the reason why more mesopore volume is obtained during the pyrolysis with H_2, and the mesopore volume grows when more H_2 is added to Ar up to 10% H_2, for which the mesopore volume saturates at about 270% relative to the mesopore volume at 0%H_2.

The volume increase of the micropores is mainly happening at defect points in the well-organized double graphene layers, for which an increase in volume by a maximum of 26% is already reached after adding 2%H_2 to Ar.

The Fe-based catalytic sites need carbon support to perform ORR in the catalysts. If the carbon support disappears due to gasification, the catalytic sites will also disappear. During the pyrolysis in forming gas, one is therefore expecting to measure (i) a significant decrease of S1 sites that are located in less graphitized carbon and form significant mesopores and; (ii) only a small variation of the S2 site content located in the double graphene layer.

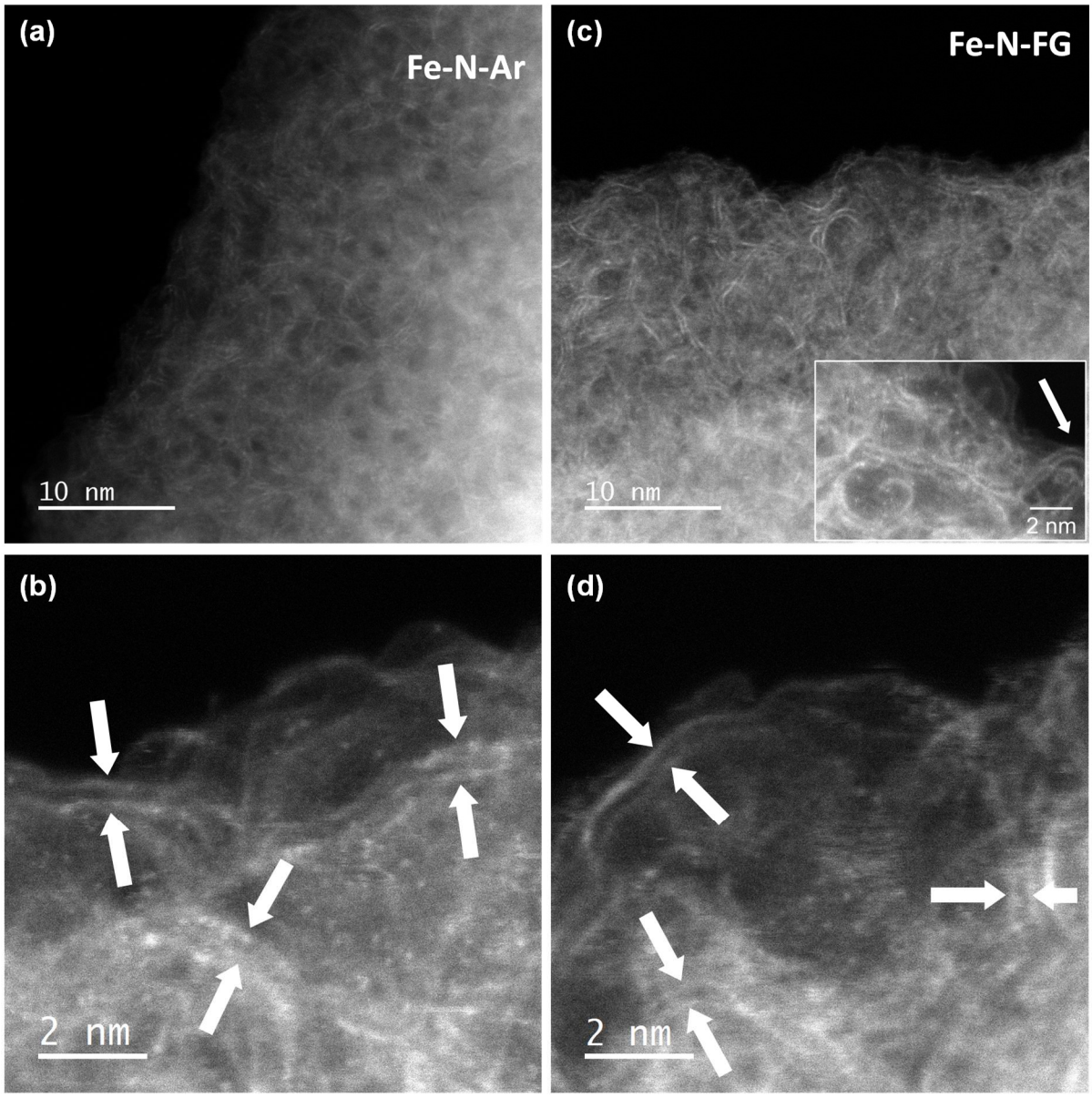

Supplementary Figure 15. Analysis of the carbon structures. Representative double-layered graphene and ill-structured carbon planes identified in the Fe-N-C-Ar (a, b) and the Fe-N-C-FG (c, d) catalysts.

Theoretical elucidation via DFT calculations

Supplementary Note 2:

Justifications of the proposed S1-4H sites are below:

Why are the 4 specific C located just next to the 4 N of the site chosen for H adsorption sites and not anywhere else?

To identify the optimal adsorption site of H on a graphene layer containing an S1 type FeN_4 site, we have compared the adsorption energies of multiple H adsorption configurations as depicted in the figure shown below. Low adsorption energy represents a strong interaction between H and the adsorption site.

Considering that protonation reactions will occur on the Fe site during ORR, the hydrogen adsorbed on Fe can be removed during ORR. Therefore, we believe that H adsorbed on Fe will not change the structure of FeN4 during ORR. We notice that the C site adjacent to the N atom is the most favorable site to adsorb the H atom, except for the Fe site. This result explains why four specific C atoms located just next to the 4 N of the site were chosen for hydrogenation.

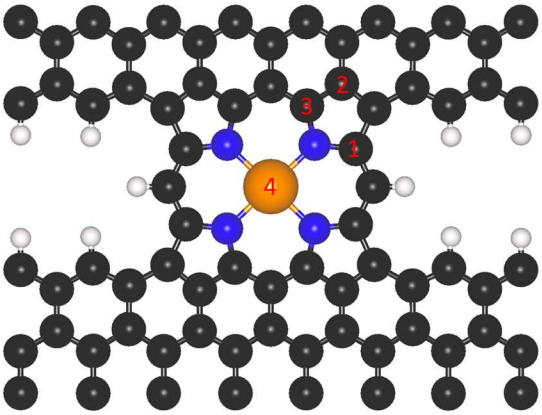

Adsorption Site	The adsorption energy of H (eV)
1	-1.50
2	-0.98
3	-1.30
4	-1.92

Supplementary Figure 16. Predicted adsorption energies of H on different sites, including carbon and iron sites. In this figure, the black, blue, orange, and white balls represent C, N, Fe, and H atoms, respectively.

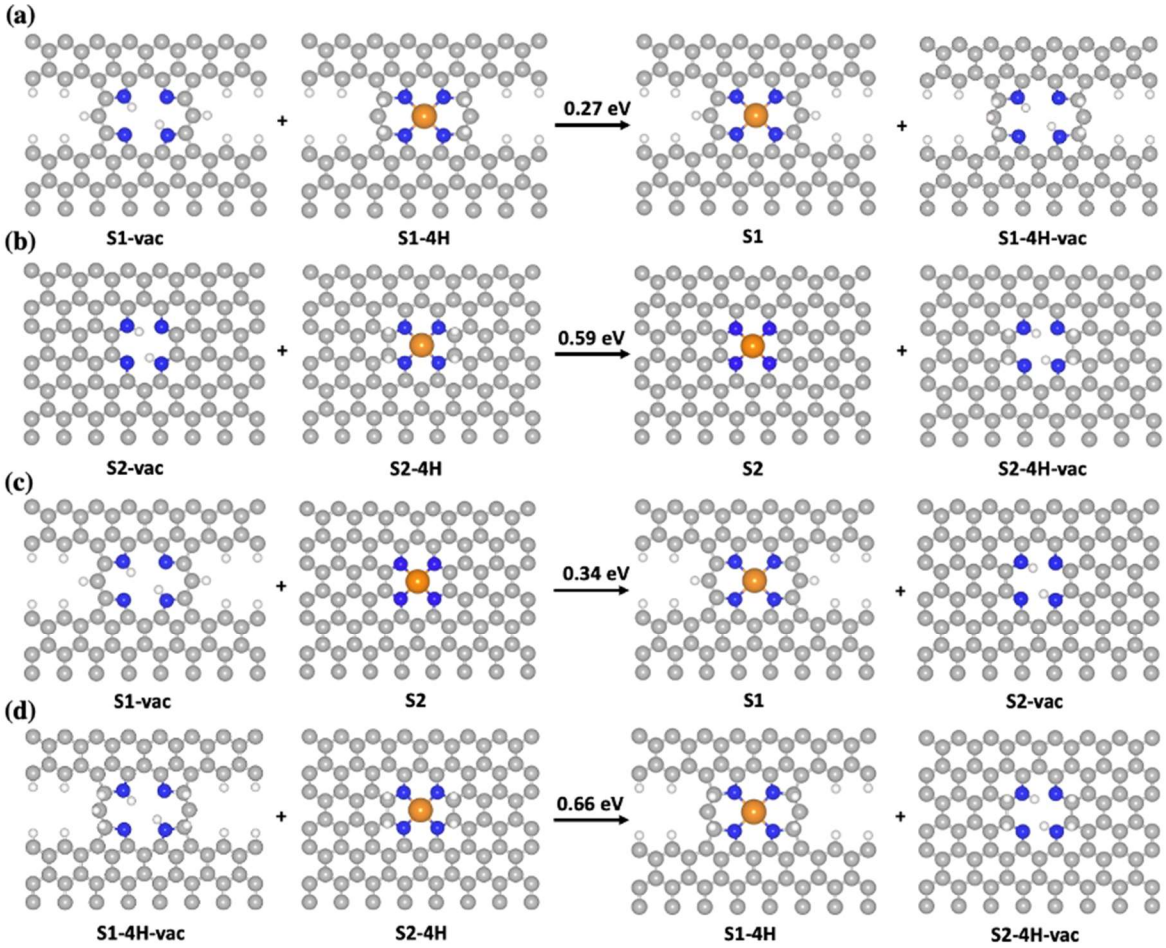

Supplementary Figure 17. Atomistic model for the transition of active sites. (a) Transition from S1-4H to S1 type N_4 moiety, (b) S2-4H to S2 type N_4 moiety, (c) S2 to S1 type N_4 moiety, and (d) S2-4H to S1-4H type N_4 moiety. In this figure, the grey, blue, orange, and white balls represent C, N, Fe, and H atoms, respectively.

Supplementary Note 3:

Moreover, we investigated how adding hydrogen would affect the stability of FeN_4 in DFT calculations. The solvation effect was included in this work using the implicit solvation model. We predicted that the free energy change for the demetallation process decreased from 0.35 eV on S1-4H to 0.05 eV on the S1 site, without considering the solvation effect (**Supplementary Table 16**). In comparison, the free energy change for the demetallation process was calculated to be 0.26 eV on the S1-4H site and −0.02 eV on the S1 site after considering the solvation effect. These results indicate that the predicted stability of the S1/S1-4H site will decrease slightly after considering the solvation effect. Still, the solvation effect would not change the relative stability between S1 and S1-4H sites. Similarly, we can make the same conclusion for the S2 site. Therefore, the introduction of the hydrogen would enhance the stability of the FeN_4 site against demetallation, and the inclusion of the solvation effect in the DFT calculations would not change the relative stability between the S1/S2 site and S1-4H/S2-4H FeN_4 sites.

Supplementary Table 16. Predicted free energy change for demetallation of central Fe from S1, S1-4H, S2, and S2-4H sites.

Active sites	**Free energy change for Demetallation (eV)**
S1	0.05
S1 (with solvation)	−0.02
S1-4H	0.35
S1-4H (with solvation)	0.26
S2	1.37
S2 (with solvation)	1.27
S2-4H	1.36
S2-4H (with solvation)	1.32

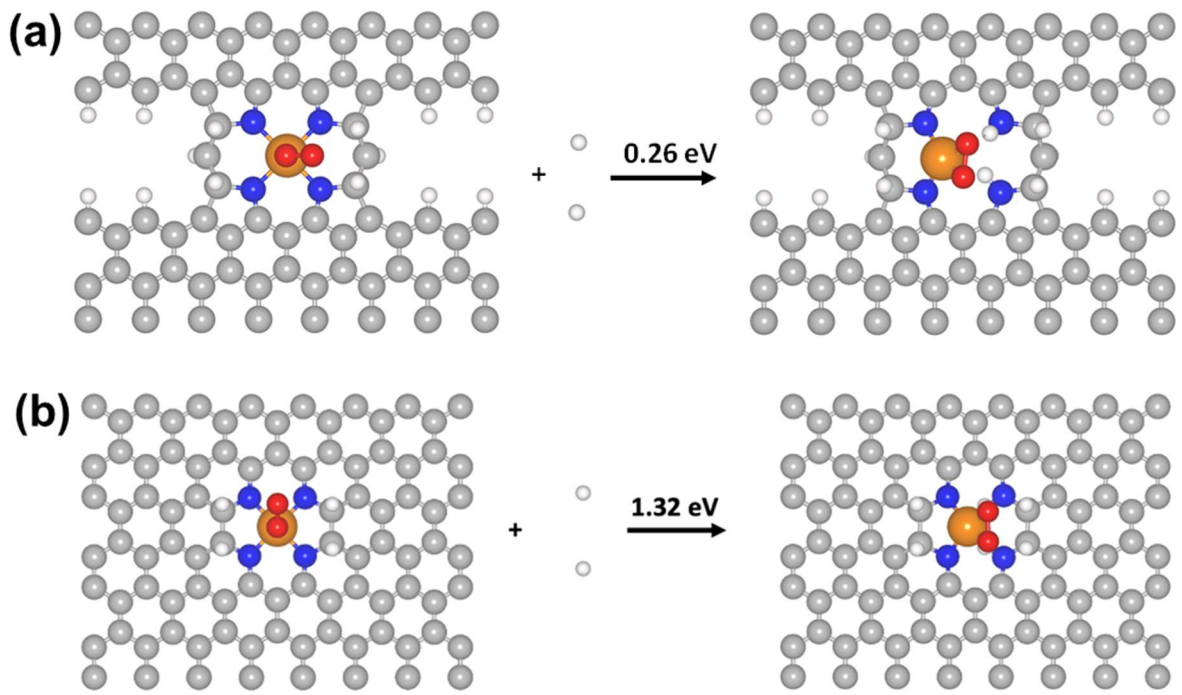

Supplementary Figure 18. Atomistic structures for demetallation of Fe from different active sites. Demetallations of Fe from S1-4H (a) and S2-4H (b) site. In the figure, the grey, blue, orange, red, and white balls represent C, N, Fe, O, and H atoms, respectively.

Supplementary Note 4:

To elaborate on why the Fe-N bond in Fe-N-C-FG catalyst is shortened as compared to that in traditional Fe-N-C catalyst, we have analyzed the electronic structure of Fe and its surrounding N atoms in the modeled S1 type FeN_4 sites. As shown in **Supplementary Figure 17**, our DFT results reveal that the $3d_{xy}$ orbital of the central Fe will overlap with the 2p orbital of the surrounding N atoms when forming the Fe-N bonds in FeN_4 moiety. It should be noted that this finding agrees well with the previous results reported for transition metal phthalocyanine molecules.[20]

Moreover, we specifically examined the density of states of the Fe $3d_{xy}$ orbital shown in **Supplementary Figure 18**. We found that this orbital is separated into two parts (i.e., a low energy part is in the range of −6 to −3 eV, and a high energy part is in the range of −1 to 3 eV) corresponding to the bonding and anti-bonding orbitals formed between Fe and its surrounding N, respectively. In this study, we proposed an S1-4H site, in which the four C atoms adjacent to the FeN_4 moiety would be covered by H because the forming gas environment used in our synthesis procedure could introduce additional H bonded with C atoms. Our DFT results in **Supplementary Figure 18** indicate that some anti-bonding orbital (*i.e.*, spin-up part) of Fe $3d_{xy}$ will participate in the Fe-N bond formation, leading to weaker Fe-N interaction and correspondingly longer Fe-N bond in the traditional FeN_4 site without adsorbed H. In contrast, only the bonding orbitals of Fe $3d_{xy}$ participate in the Fe-N bond formation, leading to stronger Fe-N interaction and correspondingly shorter Fe-N bond in our modeled S1-4H site. This result reveals that the introduction of additional H on the C atoms surrounding the FeN_4 site could modify the electronic structure of the Fe-N bonds (i.e., without the contribution from the anti-bonding orbitals to the bond formation) in the S1-4H site and thus shorten the Fe-N bonds than those in the traditional FeN_4 site.

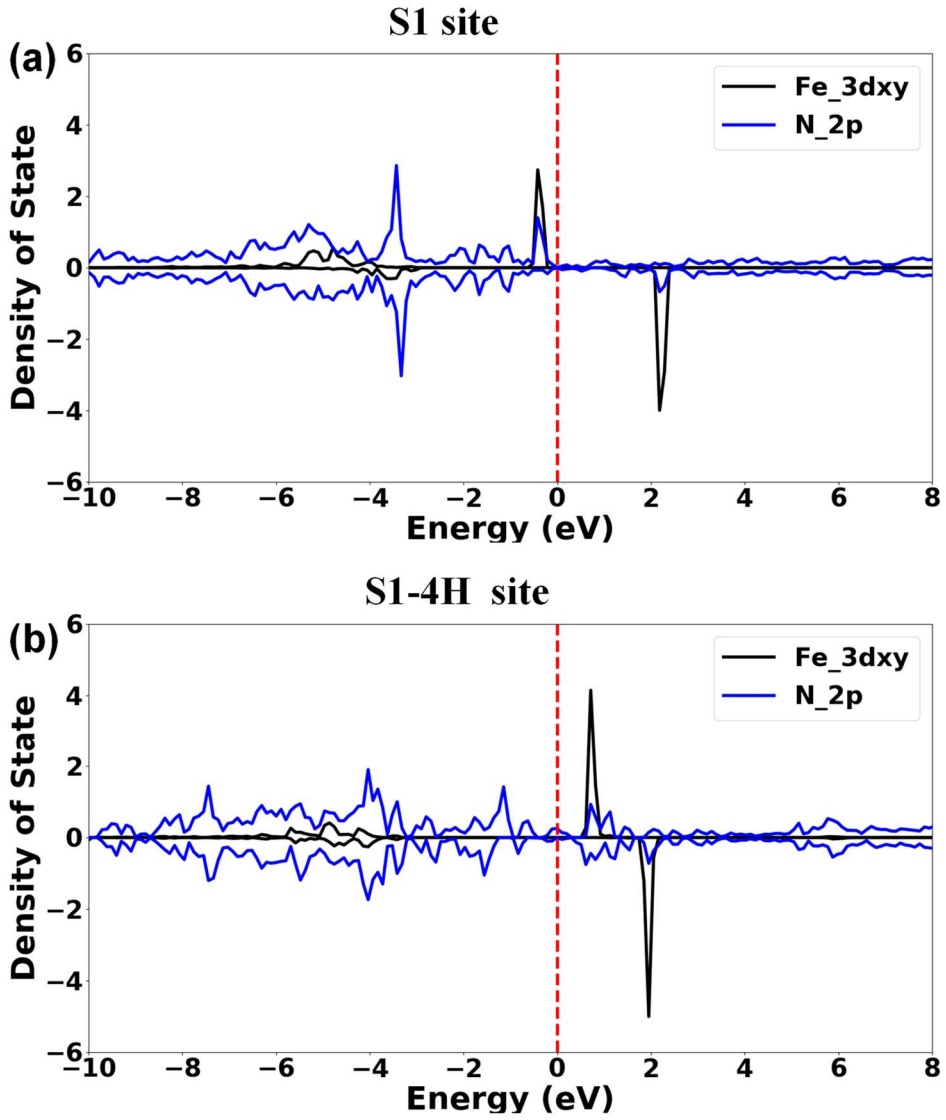

Supplementary Figure 19. Analysis of electronic structure in FeN_4. Projected density of state of $3d_{xy}$ orbital of the central Fe atom and 2p orbital of surrounding N atoms. (a) S1 type FeN_4 site and (b) S1-4H site. In the figure, the fermi energy of the investigated system was set as 0 eV.

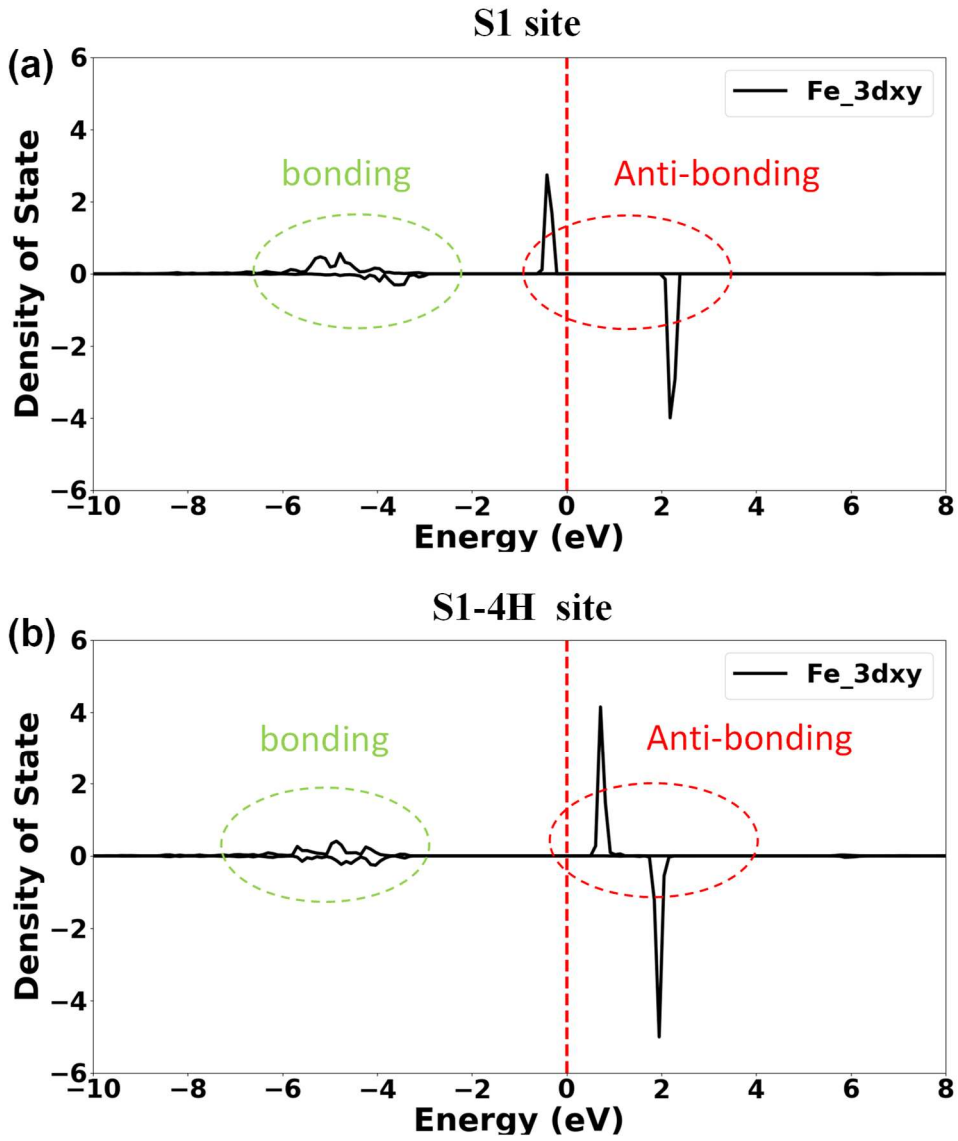

Supplementary Figure 20. Analysis of the electronic structure of S1 and S1-4H sites. Projected density of state of $3d_{xy}$ orbital of Fe atom in S1 type FeN_4 site and S1-4H site. In the figure, the fermi energy of the investigated system was set as 0 eV. At low temperatures, the states below Fermi energy will be occupied by electrons, whereas the states above Fermi energy will be unoccupied.

Supplementary Note 5:

The intrinsic catalytic activity of FeN_4 sites with/without H adsorption following the $4e^-$ associative ORR pathway was investigated. The ORR on the S1-4H site becomes an exothermic reaction when the electrode potential is lower than a limiting potential of 0.58 V, higher than that of 0.57 V on the S1 site. In addition, the ORR limiting potential was predicted to increase from 0.61 V on the S2 site to 0.67 V on the S2-4H site. These computational results indicate that introducing H would enhance the intrinsic ORR activity of FeN_4 sites. Moreover, Bader charge analysis quantitatively showed that the electron accumulation was 0.18e on the S1 type FeN_4 site and 0.37e on the S2 type FeN_4 site after hydrogen attached to carbon. Recognizing that the ORR intermediate belongs to nucleophiles, introducing surface H near the FeN_4 site will weaken the adsorption of the ORR intermediate and thus improve the overall ORR activity.

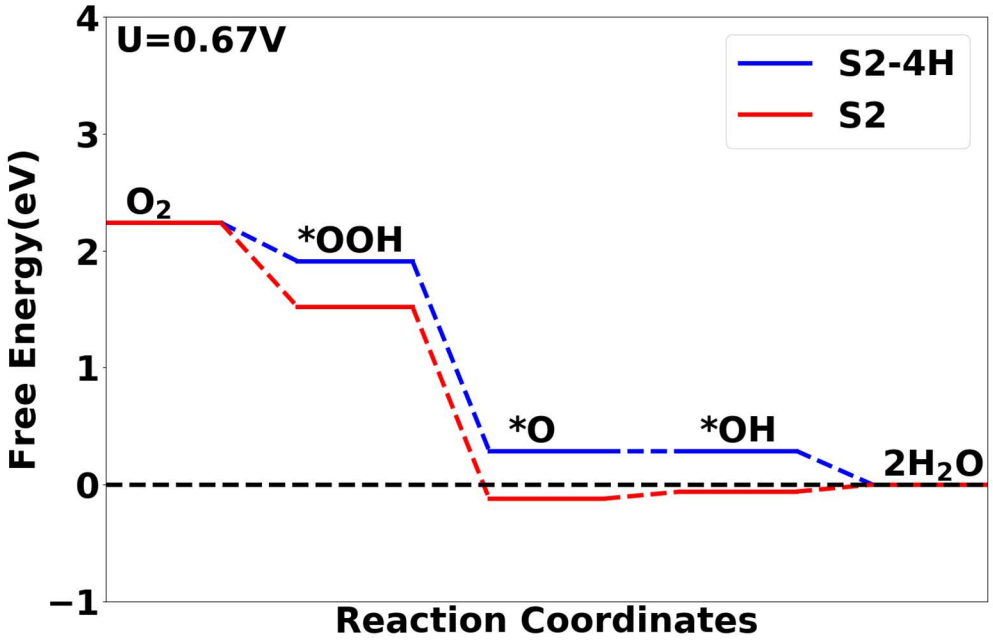

Supplementary Figure 21. Predicted free energy evolution for ORR through $4e^-$ associative pathway on S2-4H site and S2 type FeN_4 site under electrode potentials of U = 0.67 V.

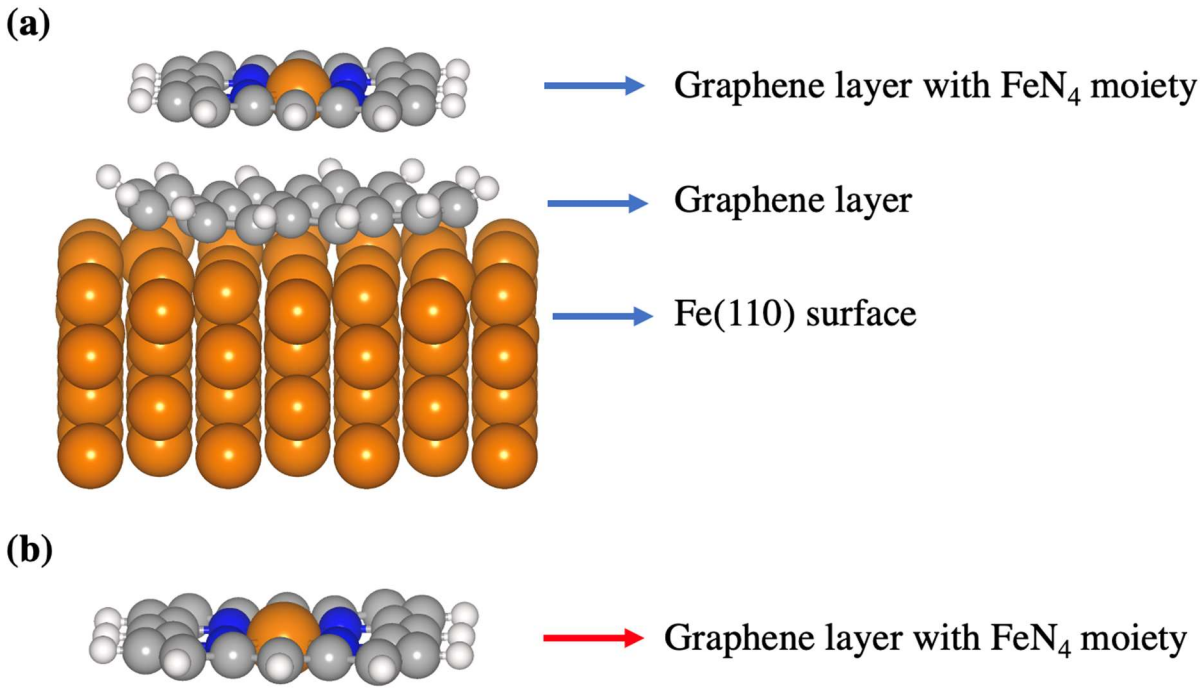

Supplementary Figure 22. Structural models for the impact of Fe nanoparticles on ORR. Atomistic structure of (a) FeN_4-G-Fe(110) and (b) FeN_4 model. In this figure, the grey, blue, orange, and white balls represent the C, N, Fe, and H atoms, respectively.

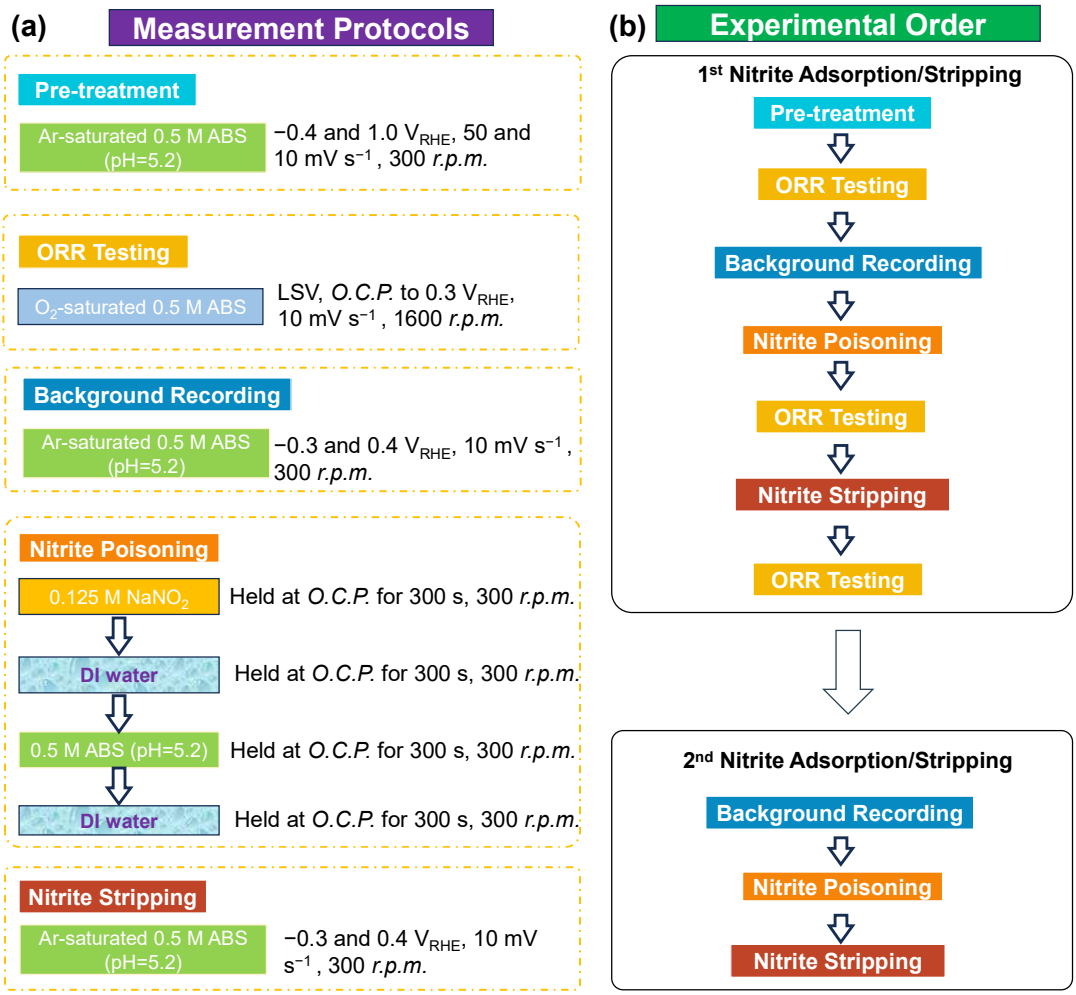

Supplementary Figure 23. The new standard protocol for the determination of FeN_4 active site density. (a) Measurement protocols used in the FeN_x site density evaluation. (b) Experimental procedures for the FeN_x site density measurement.

Supplementary References

1 Kramm, U. I. *et al.* On an Easy Way To Prepare Metal–Nitrogen Doped Carbon with Exclusive Presence of MeN4-type Sites Active for the ORR. *J. Am. Chem. Soc.* **138**, 635-640 (2016).

2 Jaouen, F. & Dodelet, J.-P. O_2 Reduction Mechanism on Non-Noble Metal Catalysts for PEM Fuel Cells. Part I: Experimental Rates of O_2 Electroreduction, H_2O_2 Electroreduction, and H_2O_2 Disproportionation. *J. Phys. Chem. C* **113**, 15422-15432 (2009).

3 Li, Q. *et al.* Highly efficient Fe-NC oxygen reduction electrocatalyst engineered by sintering atmosphere. *J. Power Sources* **449**, 227497 (2020).

4 Workman, M. J., Serov, A., Tsui, L.-k., Atanassov, P. & Artyushkova, K. Fe–N–C Catalyst Graphitic Layer Structure and Fuel Cell Performance. *ACS Energy Lett.* **2**, 1489-1493 (2017).

5 Kumar, K. *et al.* Fe–N–C Electrocatalysts' Durability: Effects of Single Atoms' Mobility and Clustering. *ACS Catal.* **11**, 484-494 (2021).
6 Li, L. *et al.* Tailoring the stability of Fe-NC via pyridinic nitrogen for acid oxygen reduction reaction. *Chem. Eng. J.* **437**, 135320 (2022).
7 Zhang, H. *et al.* Standardized protocols for evaluating platinum group metal-free oxygen reduction reaction electrocatalysts in polymer electrolyte fuel cells. *Nat. Catal.* **5**, 455-462 (2022).
8 Liu, S. *et al.* Atomically dispersed iron sites with a nitrogen–carbon coating as highly active and durable oxygen reduction catalysts for fuel cells. *Nat. Energy* **7**, 652-663 (2022).
9 Liu, S. *et al.* Chemical Vapor Deposition for Atomically Dispersed and Nitrogen Coordinated Single Metal Site Catalysts. *Angew. Chem. Int. Ed.* **59**, 21698-21705 (2020).
10 Chung, H. T. *et al.* Direct atomic-level insight into the active sites of a high-performance PGM-free ORR catalyst. *Science* **357**, 479-484 (2017).
11 Zhao, D. *et al.* Highly Efficient Non-Precious Metal Electrocatalysts Prepared from One-Pot Synthesized Zeolitic Imidazolate Frameworks. *Adv. Mater.* **26**, 1093-1097 (2014).
12 Qiao, Z. *et al.* 3D polymer hydrogel for high-performance atomic iron-rich catalysts for oxygen reduction in acidic media. *Appl. Catal. B-Environ.* **219**, 629-639 (2017).
13 Zhang, H. *et al.* High-performance fuel cell cathodes exclusively containing atomically dispersed iron active sites. *Energy Environ. Sci.* **12**, 2548-2558 (2019).
14 Wan, X. *et al.* Fe–N–C electrocatalyst with dense active sites and efficient mass transport for high-performance proton exchange membrane fuel cells. *Nat. Catal.* **2**, 259-268 (2019).
15 Tian, J. *et al.* Optimized Synthesis of Fe/N/C Cathode Catalysts for PEM Fuel Cells: A Matter of Iron–Ligand Coordination Strength. *Angew. Chem. Int. Ed.* **52**, 6867-6870 (2013).
16 Li, J. *et al.* Thermally Driven Structure and Performance Evolution of Atomically Dispersed FeN4 Sites for Oxygen Reduction. *Angew. Chem. Int. Ed.* **58**, 18971-18980 (2019).
17 Fu, X. *et al.* Tailoring FeN4 Sites with Edge Enrichment for Boosted Oxygen Reduction Performance in Proton Exchange Membrane Fuel Cell. *Adv. Energy Mater.* **9**, 1803737 (2019).
18 Li, J. *et al.* Evolution Pathway from Iron Compounds to Fe1(II)–N4 Sites through Gas-Phase Iron during Pyrolysis. *J. Am. Chem. Soc.* **142**, 1417-1423 (2020).
19 Sougrati, M. T., Goellner, V., Schuppert, A. K., Stievano, L. & Jaouen, F. Probing active sites in iron-based catalysts for oxygen electro-reduction: A temperature-dependent ^{57}Fe Mössbauer spectroscopy study. *Catal. Today* **262**, 110-120 (2016).
20 Liu, K., Lei, Y. & Wang, G. Correlation between oxygen adsorption energy and electronic structure of transition metal macrocyclic complexes. *J. Chem. Phys.* **139** (2013).